

# **NAVAL POSTGRADUATE SCHOOL**

## **Monterey, California**



## **THESIS**

**TEMPERATURE DEPENDENCE OF DARK CURRENT IN  
QUANTUM WELL INFRARED DETECTORS**

by

Thomas R. Hickey

June 2002

Thesis Advisor:  
Second Reader:

Gamani Karunasiri  
James Luscombe

Approved for public release; distribution is unlimited.

THIS PAGE INTENTIONALLY LEFT BLANK

## REPORT DOCUMENTATION PAGE

Form Approved OMB No. 0704-0188

Public reporting burden for this collection of information is estimated to average 1 hour per response, including the time for reviewing instruction, searching existing data sources, gathering and maintaining the data needed, and completing and reviewing the collection of information. Send comments regarding this burden estimate or any other aspect of this collection of information, including suggestions for reducing this burden, to Washington headquarters Services, Directorate for Information Operations and Reports, 1215 Jefferson Davis Highway, Suite 1204, Arlington, VA 22202-4302, and to the Office of Management and Budget, Paperwork Reduction Project (0704-0188) Washington DC 20503.

1. AGENCY USE ONLY (Leave blank)	2. REPORT DATE June 2002	3. REPORT TYPE AND DATES COVERED Master's Thesis
4. TITLE AND SUBTITLE: Temperature Dependence of Dark Current in Quantum Well Infrared Detectors		5. FUNDING NUMBERS
6. AUTHOR Thomas R. Hickey		
7. PERFORMING ORGANIZATION NAME(S) AND ADDRESS(ES) Naval Postgraduate School Monterey, CA 93943-5000		8. PERFORMING ORGANIZATION REPORT NUMBER
9. SPONSORING /MONITORING AGENCY NAME(S) AND ADDRESS(ES) N/A		10. SPONSORING/MONITORING AGENCY REPORT NUMBER
11. SUPPLEMENTARY NOTES The views expressed in this thesis are those of the author and do not reflect the official policy or position of the Department of Defense or the U.S. Government.		
12a. DISTRIBUTION / AVAILABILITY STATEMENT Approved for public release; distribution is unlimited.		12b. DISTRIBUTION CODE

13. ABSTRACT (*maximum 200 words*)

The *I-V* characteristics of a bound-to-continuum QWIP device with  $\text{Al}_{0.37}\text{Ga}_{0.63}\text{As}$  barriers of 23 nm,  $\text{In}_{0.1}\text{Ga}_{0.9}\text{As}$  wells of 3.6 nm, and a doping density ( $n_d$ ) of  $10^{18} \text{ cm}^{-3}$  were gathered and analyzed for various temperatures. The device was cooled with a closed cycle refrigerator, and the data were acquired using the Agilent 4155B Semiconductor Parameter Analyzer. Dark current in the device was qualitatively explained, then further examined with a thermionic emission model. Using this model and an iterative Matlab program we were able to establish the energy levels within the well. In addition, the dark current limited detectivity ( $D^*$ ) of the device was determined as a function of the temperature in the 10 – 170 K range. It was found that the  $D^*$  degrades at temperatures above 80 K due to excess thermionic emission from the quantum well.

The details of the laboratory setup and test system and process are included with the intent to provide future students with simple and comprehensive procedural insight.

14. SUBJECT TERMS Quantum well infrared photodetector, temperature dependence, dark current, thermionic emission, detectivity.		15. NUMBER OF PAGES 69	
16. PRICE CODE			
17. SECURITY CLASSIFICATION OF REPORT Unclassified	18. SECURITY CLASSIFICATION OF THIS PAGE Unclassified	19. SECURITY CLASSIFICATION OF ABSTRACT Unclassified	20. LIMITATION OF ABSTRACT UL

THIS PAGE INTENTIONALLY LEFT BLANK

Approved for public release; distribution is unlimited.

**TEMPERATURE DEPENDENCE OF DARK CURRENT IN QUANTUM WELL  
INFRARED DETECTORS**

Thomas R. Hickey  
Ensign, United States Navy  
B.A., College of the Holy Cross, 2001

Submitted in partial fulfillment of the  
requirements for the degree of

**MASTER OF SCIENCE IN APPLIED PHYSICS**

from the

**NAVAL POSTGRADUATE SCHOOL**  
**June 2002**

Author: Thomas R. Hickey

Approved by: Gamani Karunasiri  
Thesis Advisor

James Luscombe  
Second Reader

William B. Maier II  
Chairman, Department of Physics

THIS PAGE INTENTIONALLY LEFT BLANK

## ABSTRACT

The  $I-V$  characteristics of a bound-to-continuum QWIP device with  $\text{Al}_{0.37}\text{Ga}_{0.63}\text{As}$  barriers of 23 nm,  $\text{In}_{0.1}\text{Ga}_{0.9}\text{As}$  wells of 3.6 nm, and a doping density ( $n_d$ ) of  $10^{18} \text{ cm}^{-3}$  were gathered and analyzed for various temperatures. The device was cooled with a closed cycle refrigerator and the data were acquired using the Agilent 4155B Semiconductor Parameter Analyzer. Dark current in the device was qualitatively explained, then further examined with a thermionic emission model. Using this model and an iterative Matlab program we were able to establish the energy levels within the well. In addition, the dark current limited detectivity ( $D^*$ ) of the device was determined as a function of the temperature in the 10 – 170 K range. It was found that the  $D^*$  degrades at temperatures above 80 K due to excess thermionic emission from the quantum well.

The details of the laboratory setup and test system and process are included with the intent to provide future students with simple and comprehensive procedural insight.

THIS PAGE INTENTIONALLY LEFT BLANK

## TABLE OF CONTENTS

I.	INTRODUCTION.....	1
A.	INTRODUCTION.....	1
B.	STRUCTURAL CONSIDERATIONS.....	3
C.	PRESENT STATUS OF QWIPS.....	9
D.	MILITARY RELEVANCE.....	10
II.	EXPERIMENTAL .....	13
A.	TEST SETUP.....	13
B.	EXPERIMENT.....	18
C.	<i>I-V</i> AS A FUNCTION OF TEMPERATURE .....	20
III.	ANALYSIS.....	25
A.	DARK CURRENT .....	25
B.	THERMIONIC EMISSION.....	28
C.	THERMALLY GENERATED DARK CURRENT .....	33
D.	DETECTIVITY ( $D^*$ ) AS A FUNCTION OF TEMPERATURE .....	38
IV.	CONCLUSIONS.....	43
LIST OF REFERENCES .....		45
APPENDIX. [PROGRAM NOTES] .....		47
INITIAL DISTRIBUTION LIST .....		51

THIS PAGE INTENTIONALLY LEFT BLANK

## LIST OF FIGURES

Figure 1.1	The electromagnetic spectrum with the visible spectrum shown in detail.....	1
Figure 1.2	Schematic band structure of quantum-well with intersubband transitions of electrons and holes shown.....	4
Figure 1.3	MBE system in which beams of molecules or atoms are used to deposit material on a heated substrate at an ultra high vacuum condition of less than $10^{-10}$ torr base pressure .....	5
Figure 1.4	Single quantum well (a) physical structure and (b) simplified band structure.....	5
Figure 1.5	Infinite quantum well.....	6
Figure 1.6	Band diagram of bound-to-continuum quantum well structure showing the excitation of electrons to the continuum band .....	7
Figure 1.7	Band diagram of bound-to-bound quantum well structure showing the excitation of electrons and their subsequent tunneling through the barrier. ....	8
Figure 1.8	Thermal image with 640x486 pixels taken by a low-noise QWIP camera....	10
Figure 1.9	QWIP camera system.....	11
Figure 2.1	Schematic diagram of the low temperature <i>I-V</i> characterization system.....	13
Figure 2.2	Lab set up. Clockwise from “bus” (located just above the one dollar bill included for scale): temperature controller, cold head, PicoDry pump, test fixture, 4155B analyzer.....	14
Figure 2.3	Schematic diagram of the Janis Model 22 cryostat (Janis operation manual).....	15
Figure 2.4	Close in digital photograph of the cold head and Model 22 Refrigerator. Helium lines are visible at the top and run to the compressor; the wider, woven tube at the right runs to the turbopump; the “bus” with one dollar bill included for scale is in the foreground.....	16
Figure 2.5	8200 Compressor is shown to the right of the digital photo, while the Turbopump is visible to the left .....	17
Figure 2.6	Schematic of test fixture wiring highlighting the Axial Lead socket module.....	18
Figure 2.7	Channel configuration for a basic “two-pronged” device.....	19
Figure 2.8	Measured <i>I-V</i> characteristics using Agilent 4155B parameter analyzer for a 62 k $\Omega$ resistor .....	20
Figure 2.9	Measured <i>I-V</i> characteristic curve over temperature range of 10 to 170K. The symmetry of the <i>I-V</i> characteristics is due to the unipolar nature of the QWIP structure (n-i-n). .....	21
Figure 2.10	Measured leakage current as a function of temperature for 2 V across the device .....	22
Figure 2.11	Measured leakage (dark) current as a function of temperature for various biases across the device.....	22
Figure 3.1	Current as a function of bias voltage across the device at 90K.....	25

Figure 3.2	Sequential tunneling under low bias voltage.....	26
Figure 3.3	Triangular tunneling under high bias voltage. ....	26
Figure 3.4	Current as a function of bias voltage across the device at 50K, 100K, and 150K.....	27
Figure 3.5	Schematic diagram of the quantum well under an external bias showing both tunneling and thermionic processes. ....	27
Figure 3.6	Physical dimensions and orientation of the QWIP device where $L$ represents its lateral dimensions. The layers are grown along the z- direction.....	29
Figure 3.7	Schematic diagram of the two-dimensional density of states. ....	30
Figure 3.8	Arrhenius plot of the leakage current. The straight line indicates the thermionic nature of the current in the high temperature region.....	34
Figure 3.9	Linear fit of the activation energies over a range of voltages. ....	35
Figure 3.10	Conceptual diagram of the conduction band offset, $\Delta E_{C_{\max}}$ .....	37
Figure 3.11	Estimated ground state energy and conduction band offset using the thermionic emission analysis. ....	38
Figure 3.12	Photoresponse of detector at various wavelengths.....	39
Figure 3.13	Detectivity at 5 $\mu\text{m}$ versus temperature for set of bias voltages. ....	41
Figure A.1	Energy state and wavefunction in finite potential well. The finite well is extensively utilized in the design of semiconductor devices, particularly in quantum well based devices.....	47

## LIST OF TABLES

Table 3.1	Bias voltages and corresponding activation energies $V_B - E_F$ .....	35
Table 3.2	Formulas for the energy bandgaps of AlGaAs and InGaAs compounds. ....	37
Table 3.3	Device information provided by the optical experiments done by Zhou.....	39

THIS PAGE INTENTIONALLY LEFT BLANK

## LIST OF SYMBOLS

$A$	area of device
$D^*$	detectivity
$e$	electron charge
$\Delta E_C$	conduction band offset
$\Delta E_C^{\max}$	maximum conduction band offset
$E_F$	Fermi energy
$Eg$	band gap
$E_0$	ground state energy
$E_0^{\max}$	maximum ground state energy
$F(E)$	Fermi function
$\Delta f$	bandwidth
$G$	optical gain
$g(E)$	density of states
$\hbar$	reduced Planck's constant
$I_d$	dark current
$i_N$	noise current
$I_p$	photocurrent
$I-V$	current-voltage
$I(T)$	temperature dependent dark current
$k$	Boltzmann's constant
$k_{(x,y,z)}$	wave vector (in x, y, and z direction)
$L_{(w,z)}$	well width
$m_w^*$	electron effective mass in well
$n_D$	three-dimensional density of carriers in the well
$NEP$	noise equivalent power
$n(T)$	number of thermally generated charge carriers
$N_{2D}$	two-dimensional density of carriers in the well
QWIP	quantum well infrared photodetector
$R$	responsivity
$T$	temperature
$T_0$	characteristic temperature
$V_B$	barrier height
$\Phi_P$	incident power
$\psi$	wave function

THIS PAGE INTENTIONALLY LEFT BLANK

## **ACKNOWLEDGMENTS**

I am pleased to thank Professor Gamani Karunasiri, whose intelligence might only be surpassed by his kindness and generosity, for the guidance he provided me time and time again. Thanks are also due to Professor James Luscombe for his insights; to Mr. Kevin Lantz for his generous help, especially in the use of Matlab; and to Mr. Sam Barone for his electronic expertise and good humor. As always, my family deserves my utmost appreciation in many more ways than they could imagine.

THIS PAGE INTENTIONALLY LEFT BLANK

# I. INTRODUCTION

## A. INTRODUCTION

In the absence of the sun, the moon, or an artificial light source, the human eye is incapable of sight. Even on a sunny day, the eye is limited to the detection of visible light, a narrow band of the electromagnetic spectrum as illustrated in Fig. 1.1 (Johns Hopkins University spectroscopy, 1999).

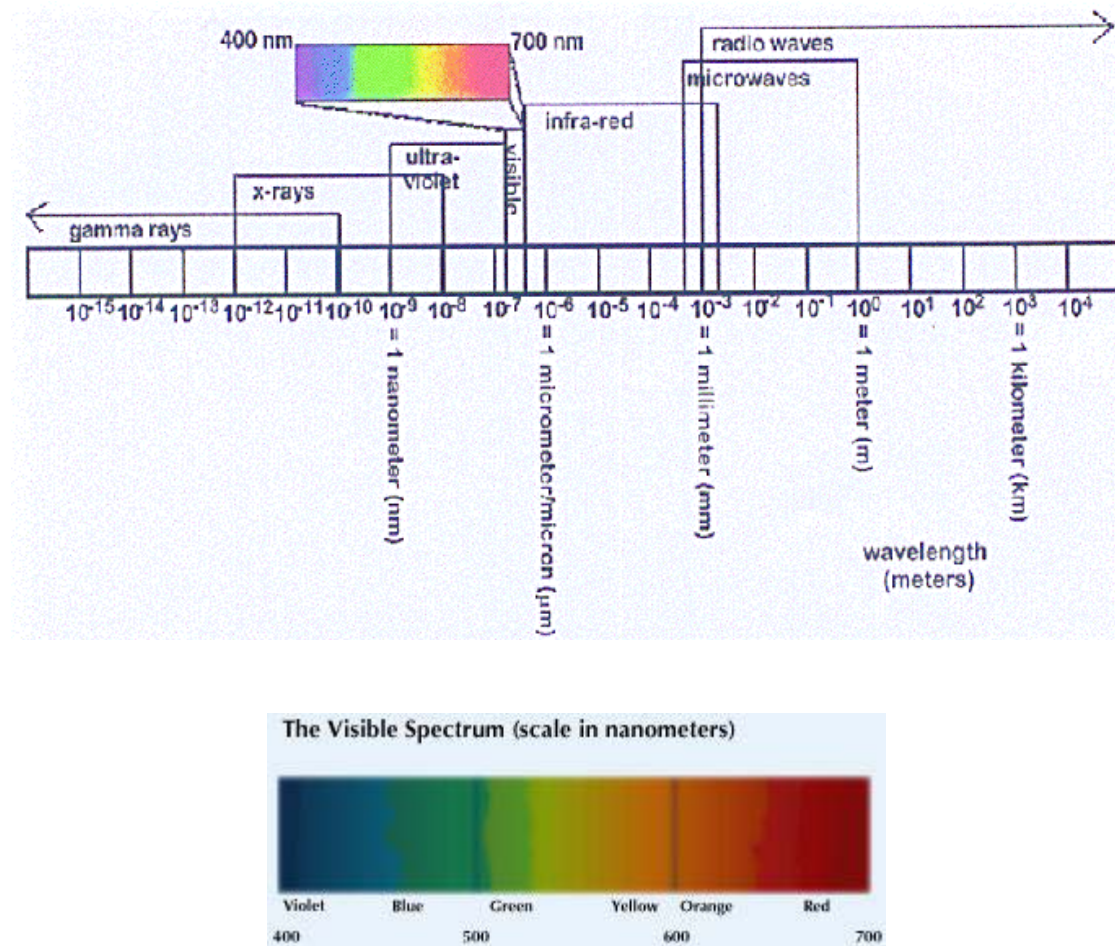


Figure 1.1 The electromagnetic spectrum with the visible spectrum shown in detail.

We detect visible light scattered from our surroundings as well as light from objects hot enough to radiate in the visible, yet anyone who has walked on a dark night knows how scarce the latter source can be. Were we able to shift our focus down the spectrum to the infrared band, however, we would observe all terrestrial objects of finite temperature with no dependence on visible light reflection. “Seeing” in the infrared is what all infrared imaging systems seek to do, and applications of this technology range from the military to the medical to the astronomical.

Infrared imaging systems operate by converting incident radiation into detectable electric signals. There are two main detection mechanisms: the thermal and the photon. Incident radiation changes the electrical properties in both types. For example, when subject to infrared radiation, thermal detectors undergo a measurable change in their electrical resistance. In addition, pyroelectric and thermoelectric effects can also be used. On the other hand, a photon detector generates electron-hole pairs, yielding a measurable photocurrent proportional to the incident radiation power. However, photon detectors must be cooled significantly to reduce the dark current associated with the thermal excitation of carriers. Despite this requirement, at low operating temperatures (less than 80 K) such devices have a responsivity and detectivity superior to that of thermal detectors (Ting, 1999, pp. 2).

Although thermal detectors are advantageous in their ability to operate near room temperature, in terms of speed and sensitivity their cooled photon detector counterparts generally prove to be the better imaging systems. The desired wavelength detection range includes important bands suffering a minimum of atmospheric absorption (3-5 and 8-12  $\mu\text{m}$ ). Furthermore, near 300 K ambient temperature blackbody radiation is brightest in the 8-12  $\mu\text{m}$  range. The 3-5  $\mu\text{m}$  detection is usually achieved by indium antimonide (InSb) and the 8-12  $\mu\text{m}$  band is covered using mercury cadmium telluride (HgCdTe, known commonly as “MCT”) detectors. The Quantum Well Infrared Photodetector (QWIP) has evolved as a useful detector in the 2-35  $\mu\text{m}$  range (Gunapala *et al.*, 2002) due to the possibility of having excellent uniformity in large area arrays. In this project, the operation parameters of a 3-5  $\mu\text{m}$  QWIP will be experimentally investigated in order to optimize its performance.

## B. STRUCTURAL CONSIDERATIONS

As previously mentioned, the important wavelength bands for infrared detection are 3-5  $\mu\text{m}$  and 8-12  $\mu\text{m}$ . The primary mechanism of the infrared photon detector is based on the photoexcitation of charge carriers across a band gap,  $E_g$ . The longer the detection wavelength, the narrower a band gap is required. From our extensive experience with visible light (roughly 400-800 nm) we know that silicon (Si,  $E_g = 1.1 \text{ eV}$ ) has shown to be an ideal detector of it. However, the difficulty of making adequate detectors for the desirable infrared wavelengths results from the lack of materials having band gaps in the 0.1 – 0.4 eV range.

Though materials such as InSb ( $E_g = 0.2 \text{ eV}$ ) and mercury cadmium telluride (HgCdTe,  $E_g = 0.1 \text{ eV}$ ) have sufficiently small band gaps, they ordinarily present difficulties in their material stability, uniformity, and reproducibility, particularly in comparison with larger-band-gap devices such as Si and gallium arsenide (GaAs). This difficulty prompted the use of heterostructures made of large gap semiconductors in the fabrication of infrared detectors (Levine, 1993, pp. R3). An AlGaAs/GaAs heterostructure and the resulting well structure are illustrated schematically in Fig. 1.2.

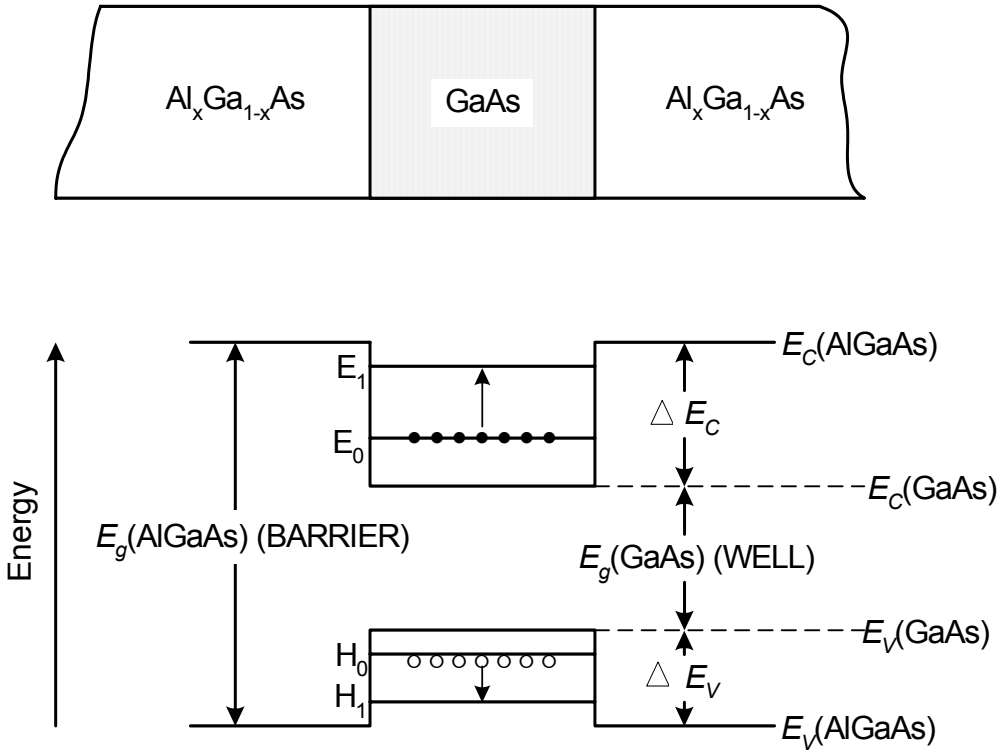


Figure 1.2 Schematic band structure of quantum-well with intersubband transitions of electrons and holes shown.

A typical QWIP is composed of alternating layers of two different semiconductors. A thin layer of a smaller bandgap semiconductor (i.e. GaAs) is placed between two layers of a larger bandgap material (i.e.  $\text{Al}_x\text{Ga}_{1-x}\text{As}$ ), thus creating a quantum well. Such a structure can be obtained by growing the layers alternately using Molecular Beam Epitaxy (MBE) or Metal Organic Vapor Deposition (MOCVD). The growth of thin layers using MBE is schematically depicted in Fig. 1.3.

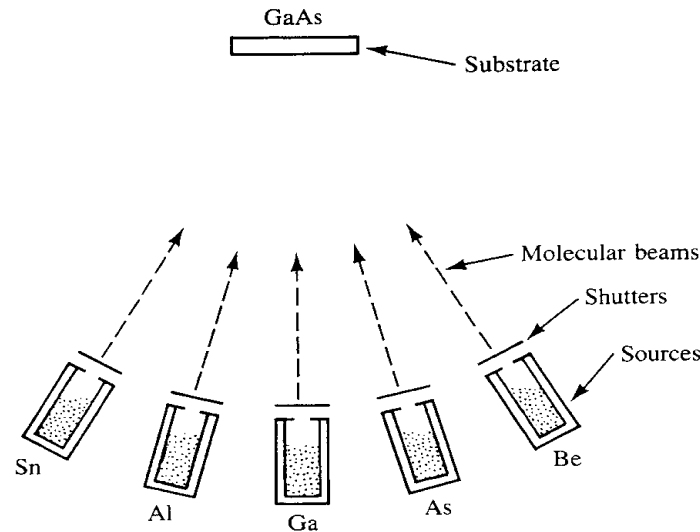


Figure 1.3 MBE system in which beams of molecules or atoms are used to deposit material on a heated substrate at an ultra high vacuum condition of less than  $10^{-10}$  torr base pressure.

The question still remains: How can large band gap materials such as Si and GaAs be used to detect the relatively long infrared wavelengths? In a quantum well, absorption results in transitions between the quantized energy states within the same band (intersubband) rather than the more familiar transition between the valence and conduction bands (interband). That is, the QWIP detects infrared radiation by exciting bound electrons within the quantum wells created in the heterostructure. Both the physical situation and the intersubband transition are shown in Fig. 1.4.

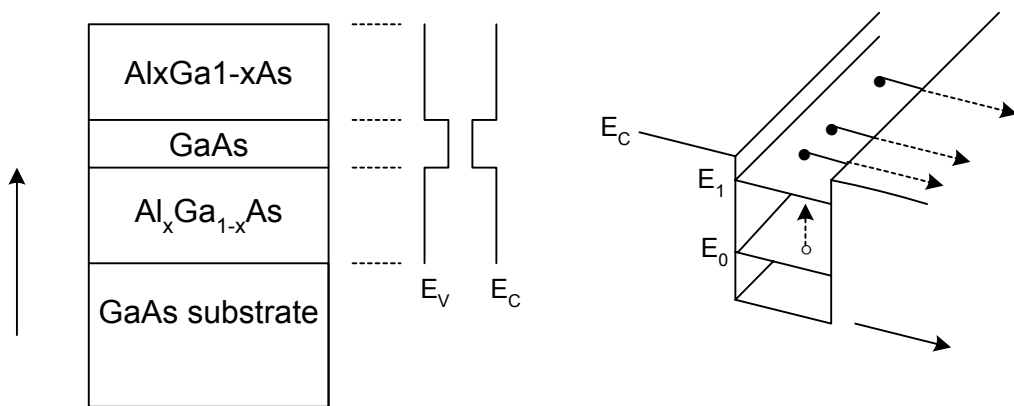


Figure 1.4 Single quantum well (a) physical structure and (b) simplified band structure.

A common and useful starting point in describing the quantum well structure is to postulate the infinite quantum well. Solving the Schrödinger equation in this case is straightforward due to the conditions that the wave function must go to zero at the boundaries and that because of the infinite potential of the walls, the electron must be confined within the well. A schematic description of the infinite quantum well is given in Fig. 1.5. The one-dimensional Schrödinger equation is as follows:

$$\frac{-\hbar^2}{2m_w^*} \frac{d^2\psi(z)}{dz^2} + V(z)\psi(z) = E_z\psi(z) \quad (1.1)$$

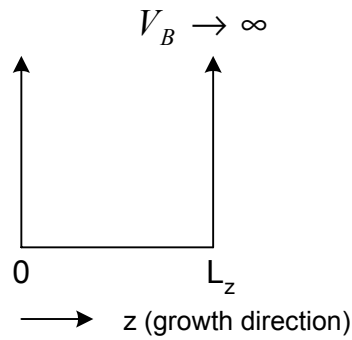


Figure 1.5     Infinite quantum well.

In Eq. (1.1),  $m_w^*$  is the electron effective mass in the well,  $V(z)$  is the potential distribution,  $\hbar$  is the reduced Planck's constant. Solving the Schrödinger equation, the eigenfunctions  $\psi(z)$  and the eigenenergies  $E_z$  are as follows:

$$\psi(z) = \sqrt{\frac{2}{L_z}} \sin(k_z z), \quad (1.2)$$

where  $k_z$  is the wave vector in the growth direction ( $z$ ) and is given by

$$k_z = \frac{n\pi}{L_z}, \quad (1.3)$$

and

$$E_z = \frac{\hbar^2 k_z^2}{2m_w^*}. \quad (1.4)$$

It can be seen that the eigenenergy between the first and second energy level is dependent on  $L_z$ . Thereby the well width becomes an important design parameter used to select the wavelength a given QWIP “sees”. In addition, the width of the well also determines the location of the excited state relative to the barrier height in the case of a finite potential. There are two principle types of QWIP, each determined by the location of the excited state: bound-to-bound and bound-to-continuum. The QWIP studied in this thesis is a bound-to-continuum type.

In a bound-to-continuum QWIP, the required detector wavelength is obtained by adjusting the well width such that the first energy level occurs in the well and the subsequent states form a continuum band just above the well as illustrated in Fig. 1.6.

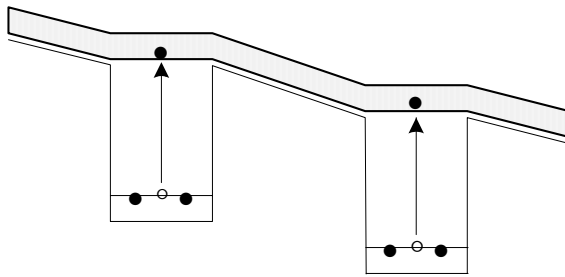


Figure 1.6 Band diagram of bound-to-continuum quantum well structure showing the excitation of electrons to the continuum band.

Thus, when a photon is incident with energy at least equal to the energy difference between the first bound state and the continuum state, it will be absorbed by an electron in the well that will undergo a transition to the continuum band. If a bias is placed across the device, the excited electron drifts under the field, forming a photocurrent proportional to the initial incident infrared radiation intensity.

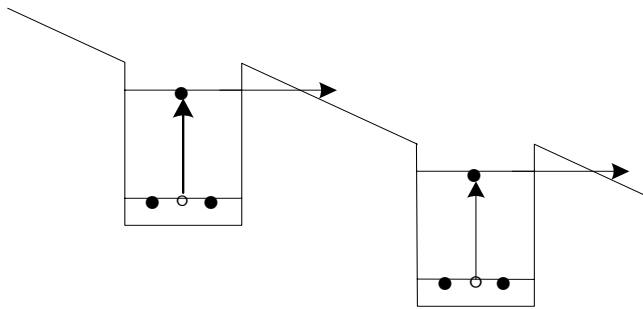


Figure 1.7 Band diagram of bound-to-bound quantum well structure showing the excitation of electrons and their subsequent tunneling through the barrier.

In a bound-to-bound quantum well structure, shown schematically in Fig. 1.7, electrons are excited from the first bound state to the second bound state, then tunnel out through the barrier under an applied electric field and form a photocurrent. The well parameters are designed such that the barriers are thick enough to reduce the tunneling current through the ground levels (i.e., up to 500 Å). The excited electrons then tunnel through the triangular barrier formed due to the external bias (see Fig. 1.7). Furthermore, the position of the excited state is based on several considerations: the transport of photoelectrons, the absorption strength, and the dark current. The main limitation of QWIP devices is the presence of this dark current, which limits the detectors' sensitivities at higher operating temperatures.

Generally, the intrinsic electron concentration in the well is too low for the generation of sufficient photocurrent. Hence, the wells are typically doped with silicon to provide adequate charge carriers. At room temperature these carriers easily “boil off” due to thermal excitation, forming a large dark current even in the absence of incident radiation. It is because of this thermionic emission and the consequent dark current that we must cool the QWIP to a low temperature for it to be an effective detector.

Countless combinations of factors ranging from the material properties of the semiconductors to the consideration of operational temperature underlie the difficult task of establishing the optimal structural and operating parameters for a specific QWIP application. Researchers have been working on these matters for nearly thirty years (Levine, 1993, pp. R3).

### C. PRESENT STATUS OF QWIPS

Before the availability of modern growth techniques, Esaki *et al.* proposed research on the quantum effects of semiconductor heterostructures in 1969. The use of larger-band-gap heterostructures as an alternative to the inadequate InSb and HgCdTe type devices was first proposed by Esaki and Sakaki in 1977. A number of experimental (Smith *et al.* and Chiu *et al.*, both 1983) and theoretical (Coon, Karunasiri, and Liu, 1984 and 1985) investigations followed, leading up to the first observation of strong intersubband absorption in GaAs/AlGaAs quantum wells by West *et al.* in 1985.

The earliest working QWIP was designed soon after by Levine *et al.* (1987). Again, it was a GaAs/AlGaAs device and was based on bound-to-bound transitions. The photoelectrons in this first device had to tunnel through relatively large barriers, a limitation that yielded an extremely low responsivity. Bound-to-bound shortcomings led to the use of bound-to-continuum transitions, which were first proposed by Coon and Karunasiri in 1984. The first bound-to-continuum QWIP was demonstrated to have a much higher responsivity (Hasnain *et al.*, 1989), but also a small peak absorbance due to the weak oscillator strength above the well.

Further advances in QWIP design have led to structures that are based on bound-to-quasi-continuum transitions (Levine *et al.*, 1991), bound-to-miniband transitions (Yu *et al.*, 1991) and bound-to-quasi-bound transitions (Gunapala *et al.*, 1996). These more recent configurations have shown good detector performance due to the fact that in all of these cases the ground state electrons do not flow in response to an external bias while the photoelectrons can create a photocurrent with the use of a relatively small bias. Multiple structural optimizations have also been made that improve QWIP performance.

Increasing the barrier width has reduced the tunneling current by many orders of magnitude (Levine *et al.*, 1991) while lowering the excited state from the continuum into the quasi-bound region has been shown to reduce the dark current from thermionic emission by a factor of roughly 12 at 70K (Gunapala *et al.*, 1996). It has also been found that adding a grating on top of the device and thereby increasing the electric field

polarization normal to the quantum wells substantially increases absorption strength (Gunapala *et al.*, 1996).

#### D. MILITARY RELEVANCE

The QWIP is of particular relevance in today's military because of its capabilities as both an infrared imager and as a laser spot tracker for use in laser-guided weapons delivery. Quantum well structures can be designed capable of detecting wavelengths as low as 1  $\mu\text{m}$ , and as such they can be tuned to detect standard NATO/U.S. combat laser designation wavelengths. In addition to this powerful capability, quantum wells can be tuned to detect infrared radiation in the 8-10  $\mu\text{m}$  window, which for the reasons previously mentioned make it useful as an infrared imager. The picture shown in Fig. 1.8 is an example of the impressive capability of a QWIP camera system like the one shown in Fig. 1.9 (both taken from Fraunhofer Institute's 2001 Annual Report):



Figure 1.8 Thermal image with 640x486 pixels taken by a low-noise QWIP camera.



Figure 1.9 QWIP camera system.

Military applications of infrared and laser detection technology are numerous. Specific benefits of QWIP devices are immediately evident in the following case: Military airborne weapon systems often utilize a FLIR (Forward Looking InfraRed) for target acquisition and tracking, as well as a laser target designator/range finder. The two are often co-located in a single weapons pod as in the case of LANTIRN (Low Altitude Navigation and Targeting Infrared for Night).

Some aircraft, such as the F-18, also employ a laser spot tracker located in a separate, externally mounted pod. The addition of the separate laser spot tracker (LST) provides the pilot with a visual laser designation cue, which is especially useful when designation occurs from an offboard source (i.e. special operations and “buddy lasing”). The LST affords much greater accuracy and confidence in ordinance delivery while expanding employment options.

Infrared sensing technology is also being employed for the purposes of free space communication. Many hand held “personal digital assistants” (PDAs) already transfer data using infrared beaming. Meanwhile, current battlefield communications rely on radio frequency (RF) technologies. Despite its longstanding effectiveness, RF communication is susceptible to intercept, jamming, and detection. Research is currently being done on the possibility of employing laser diodes operating in the high

transmission mid-wave infrared (MWIR)  $3 - 5 \mu\text{m}$  range to provide very high bandwidth free space optical communication.

The medical market for QWIP technology is also of obvious interest to the military. Breast cancer detection is only one example of QWIP medical applicability. In this case, slight changes of the skin temperature in the vicinity of a tumor can be detected. Fraunhofer IAF reports that to achieve this end, thermal deviations with a modulation frequency of  $0.1 - 2 \text{ Hz}$  must be detected. Clearly infrared and laser technology is at the heart of many critical military applications. As this promises to be the case well into the future, QWIP applications will continue to be of significant interest to the military.

## II. EXPERIMENTAL

### A. TEST SETUP

The title of this thesis disguises one of the main purposes of my work, which was to set up a low temperature current-voltage ( $I-V$ ) measurement system. The task of supply gathering and setup proved considerably more difficult than finally running the experiment. Consequently, this section is tantamount to an operational manual describing that portion of the lab pertaining to my research. It is my hope that it will be useful to future students.

The experimental setup for the measurement of  $I-V$  characteristics under varying temperature is given schematically in Fig. 2.1 and the various components are described in detail below.

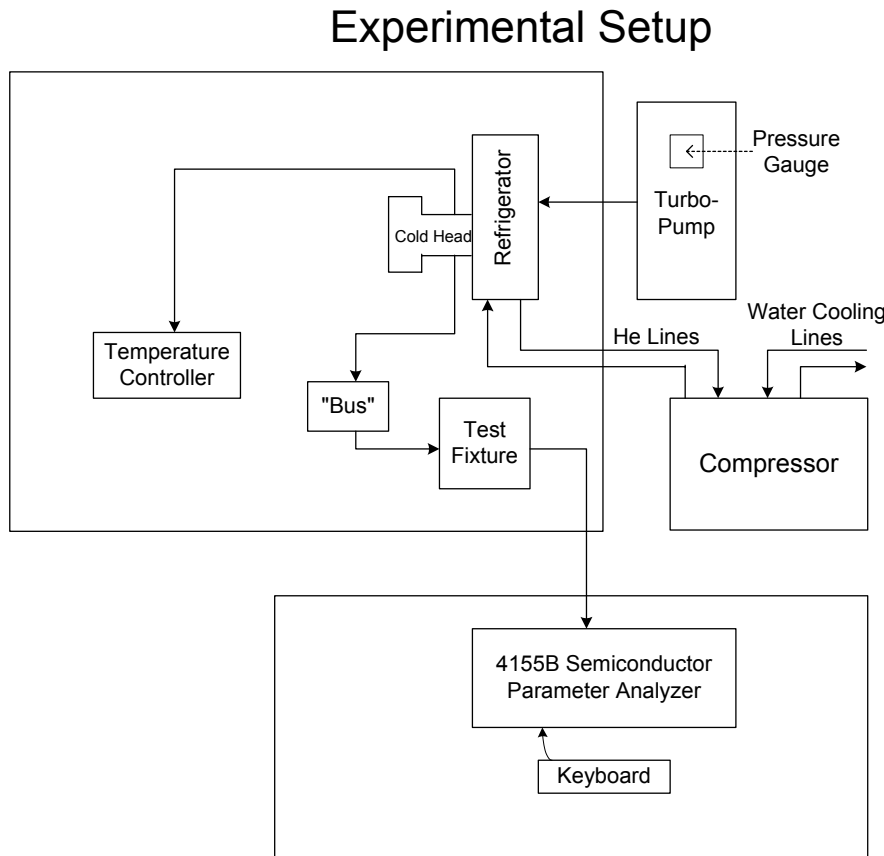


Figure 2.1 Schematic diagram of the low temperature  $I-V$  characterization system.

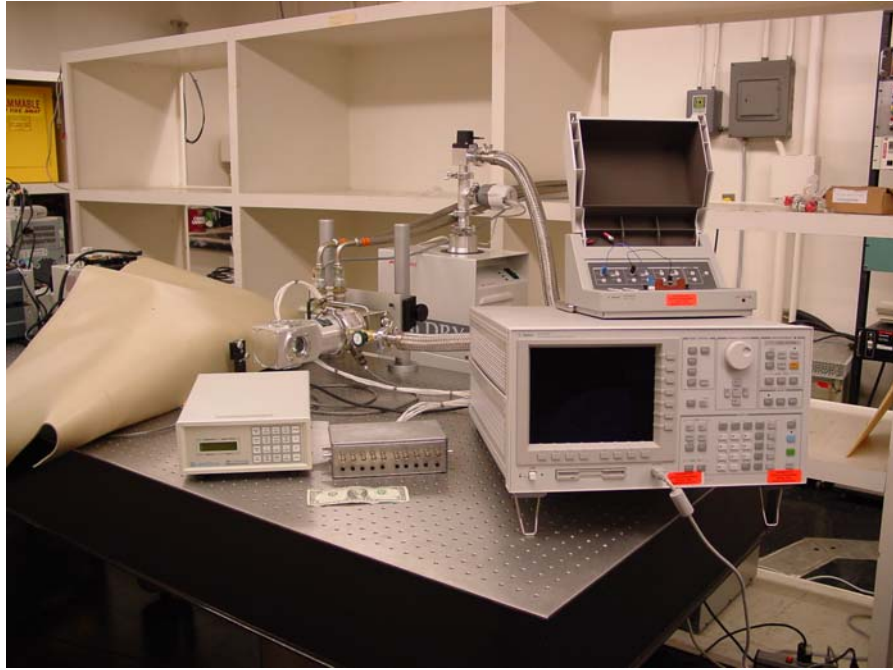


Figure 2.2 Lab set up. Clockwise from “bus” (located just above the one dollar bill included for scale): temperature controller, cold head, PicoDry pump, test fixture, 4155B analyzer.

Laboratory Equipment:

Agilent 4155B Semiconductor Parameter Analyzer

Agilent 16442A Test Fixture

CTI-Cryogenics [Helix Technology Corporation] 8200 Compressor

CTI Model 22 Refrigerator

Janus CCR cold head, Model No. CCS-150, Serial No. 7836

Lake Shore 321 Autotuning Temperature Controller

Edwards PicoDry Turbomolecular Pump, TA1A-12-042

Electrical “Bus,” assembled with the assistance of Mr. Sam Barone.

The device under test must be carefully mounted in the cold head (see Fig's. 2.3 and 2.4) to prevent dust and oils from tainting the system. Inside the cold head, ten lengths of RG-178 coaxial cable were soldered to the output. Fastened to these cables were clasps small enough to grasp the pins of the ceramic package used for mounting the QWIP devices. An electrical "bus" was created as a sampling platform to accommodate any number of simultaneous experiments being carried out on multiple devices. The signal from the cold finger runs directly to this bus, which is then connected to the test fixture of the 4155B semiconductor parameter analyzer. The 4155B can be used to sweep either voltage across the device or current through it while measuring the current and voltage. The data is automatically recorded in the memory and can be stored either in the internal hard disk or in a floppy disk for further analysis.

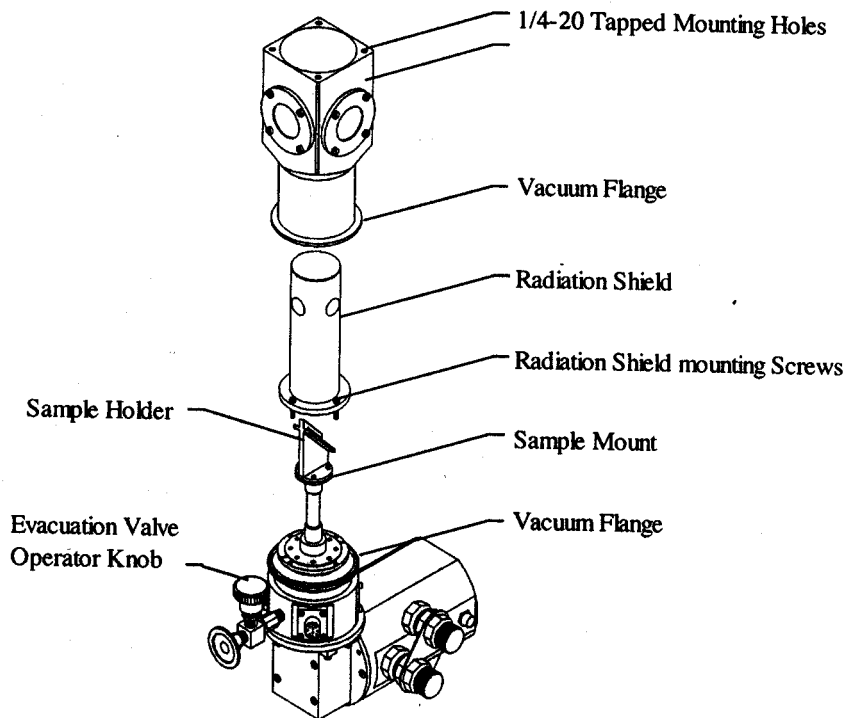


Figure 2.3 Schematic diagram of the Janis Model 22 cryostat (Janis operation manual).



Figure 2.4 Close in digital photograph of the cold head and Model 22 Refrigerator. Helium lines are visible at the top and run to the compressor; the wider, woven tube at the right runs to the turbopump; the “bus” with one dollar bill included for scale is in the foreground.

It has been stated that the operational temperature regime of a QWIP device must be relatively low for the device to be useful. Thus we require a closed cycle refrigerator utilizing a compression-expansion cooling process analogous to a common household refrigerator. Unlike the latter system, however, the Model 22 Refrigerator employs a cyclic flow of helium gas through various compression-expansion stages. The compressed helium gas is supplied by the water-cooled CTI 8200 Compressor shown in Fig. 2.5.



Figure 2.5     8200 Compressor is shown to the right of the digital photo, while the Turbopump is visible to the left.

Before beginning the refrigeration process, we must draw a vacuum in the cold head in order to remove the air inside the vacuum jacket, thus preventing condensation on the external surface. To achieve low pressures in the jacket, we employ the PicoDry Turbomolecular pump (see Fig. 2.5), which is fully automatic and quickly achieves pressure of about  $10^{-5}$  Torr, which is displayed on the Active Gauge Controller. This AGC is wired to the Wide Range Gauge, the instrument that actually measures pressure. All together, the pumping system is highly effective and simple to operate.

Once the vacuum is established, the compressor and the closed cycle refrigerator work together to extract heat from the cold head, a process visible on the temperature controller. Once we reach our baseline temperature (roughly 8K) we can begin to adjust the temperature solely via the temperature controller, which can activate the heating coil attached to the cold head.

## B. EXPERIMENT

In order to familiarize oneself with the 4155B Semiconductor Parameter Analyzer, it is best to begin with a resistor or diode. As an illustrative example, take the resistor. Assuming that the analyzer is properly wired to the test fixture (see “Quick Start Guide” 2-5), turn on the machine and observe the “Channel Definition” screen. The so-called “axial lead” socket module is convenient for the mounting of simple two prong devices, and is schematically drawn below in Fig. 2.6.

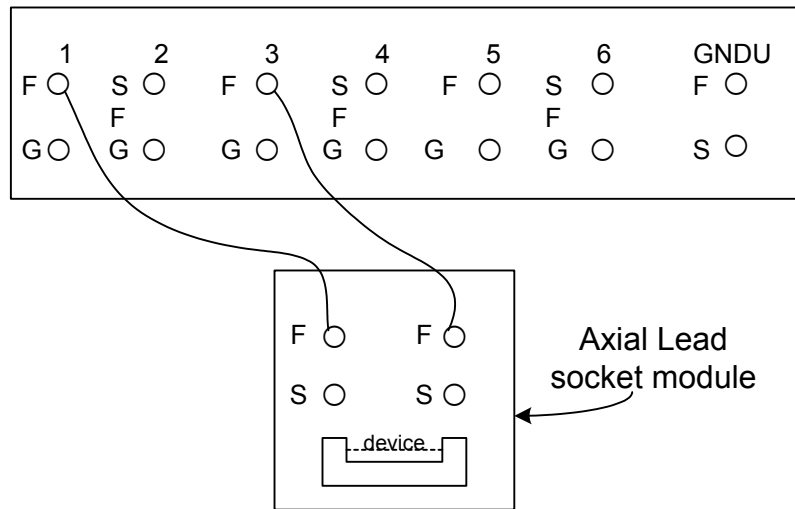


Figure 2.6     Schematic of test fixture wiring highlighting the Axial Lead socket module.

For such a device, we need only two Source/Monitor Unit (SMU) channels. Thus, our channel screen looks roughly like the arrangement shown below in Fig. 2.7:

CHANNELS: CHANNEL DEFINITION

\*MEASUREMENT MODE

SAMPLING

\*CHANNELS

MEASURE					STBY
UNIT	VNAME	INAME	MODE	FCTN	
SMU1:MP	VF	IF	V	VAR1	
SMU2:MP					
SMU3:MP	V	I	COMMON	CONST	
SMU4:MP					
SMU5:MP					
SMU6:MP					
VSU1					
VSU2					
VMU1					
VMU2					
PGU1					
PGU2					
GNDU					

Figure 2.7 Channel configuration for a basic “two-pronged” device.

This same configuration can also be arrived at by simply pushing the “MEM4 / DIODE / VF-IF” memory softkey. Continue by pushing the “next page” softkey, which calls up first the “USER FUNCTION DEFINITION,” then the “SWEEP SETUP,” and finally the “DISPLAY SETUP” pages, on which we can define names, units, etc.; change the increments of the sweep; and alter graph range and domain, respectively. For the simple purpose of successfully viewing the *I-V* characteristics of the resistor, we can simply bypass these screens. On the “GRAPH” page, press the “SINGLE” button in the upper right-hand side of the panel to test the device. The cursor should move across the screen leaving a yellow line. To adjust the scaling, simply press the “SCALING” and

then the “AUTO SCALING” softkeys. This should yield the linear lineshape we expect from a resistor as illustrated in Fig. 2.8.

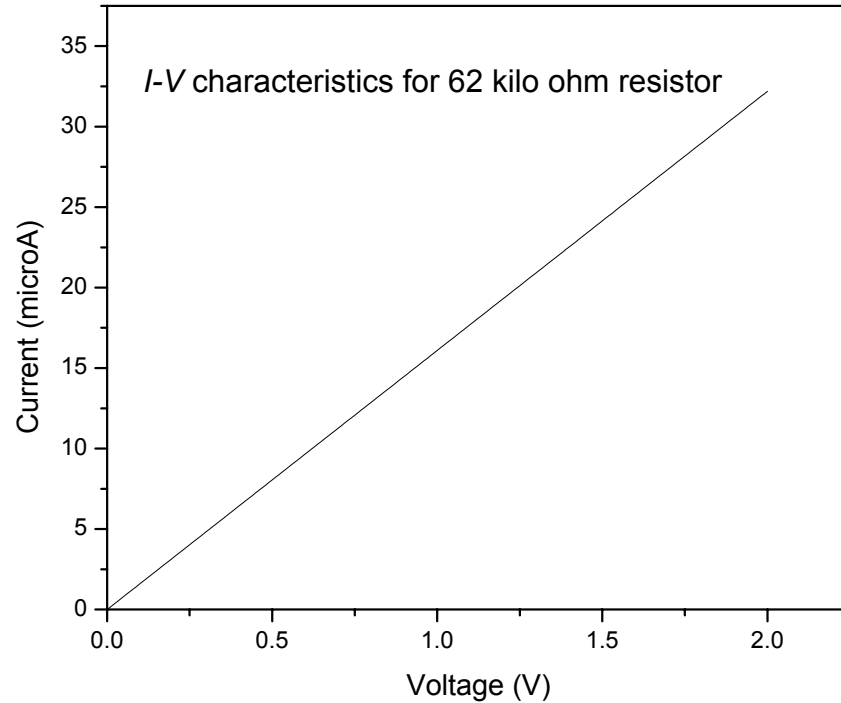


Figure 2.8 Measured  $I$ - $V$  characteristics using Agilent 4155B parameter analyzer for a  $62\text{ k}\Omega$  resistor.

For a QWIP, the process is remarkably similar, with an identical channel arrangement except that the signals come from the external bus rather than from the socket module within the test fixture.

### C. $I$ - $V$ AS A FUNCTION OF TEMPERATURE

The purpose of this project is to carry out a detailed study of the dark condition  $I$ - $V$  characteristics of an AlGaAs/InGaAs, 3-5  $\mu\text{m}$  QWIP as a function of temperature in order to determine the quantized energy levels and performance parameters. The QWIP structure used in this study consists of 25 periods of 23 nm thick  $\text{Al}_{0.37}\text{Ga}_{0.63}\text{As}$  barrier and 3.6 nm well. The entire quantum well structure is sandwiched between 1  $\mu\text{m}$  GaAs buffers and 0.5  $\mu\text{m}$  GaAs cap layers, which are doped to  $10^{18}\text{ cm}^{-3}$ . The  $I$ - $V$  measurement

was carried out over a temperature range of 10 to 170 K using 200 by 200  $\mu\text{m}^2$  mesa diodes.

Measured  $I$ - $V$  characteristics of the QWIP sample between 10 and 170 K are shown in Fig. 2.9. During the measurement, the device was covered using a cold shield to eliminate the photocurrent generated by background thermal radiation. The  $I$ - $V$  characteristics shown in Fig. 2.9 are relatively insensitive to temperature below 80 K, while in the high temperature regime they show strong temperature dependence. The dramatic reduction of the dark current at low temperatures is largely due to the decrease of thermionic emission.

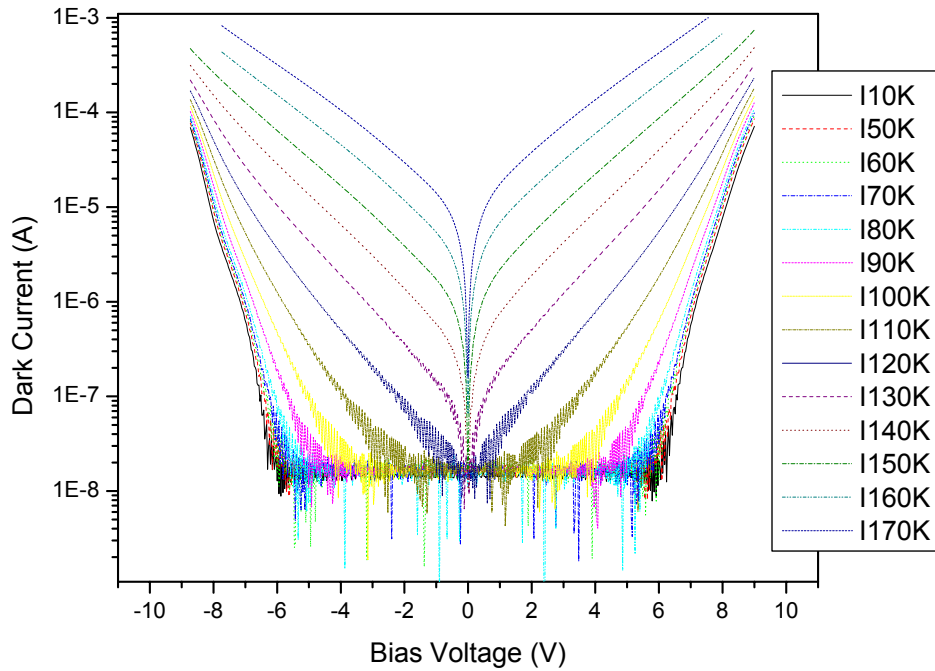


Figure 2.9     Measured  $I$ - $V$  characteristic curve over temperature range of 10 to 170K.  
The symmetry of the  $I$ - $V$  characteristics is due to the unipolar nature of the QWIP structure (n-i-n).

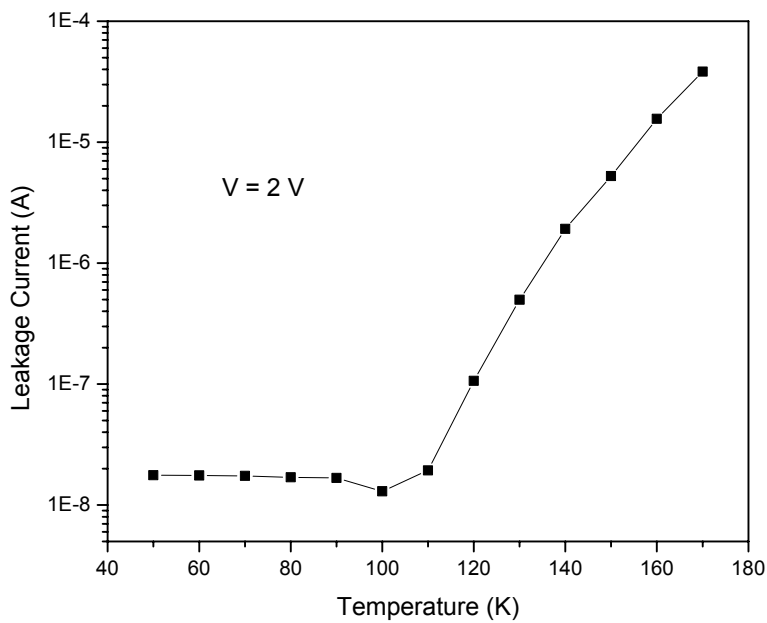


Figure 2.10 Measured leakage current as a function of temperature for 2 V across the device.

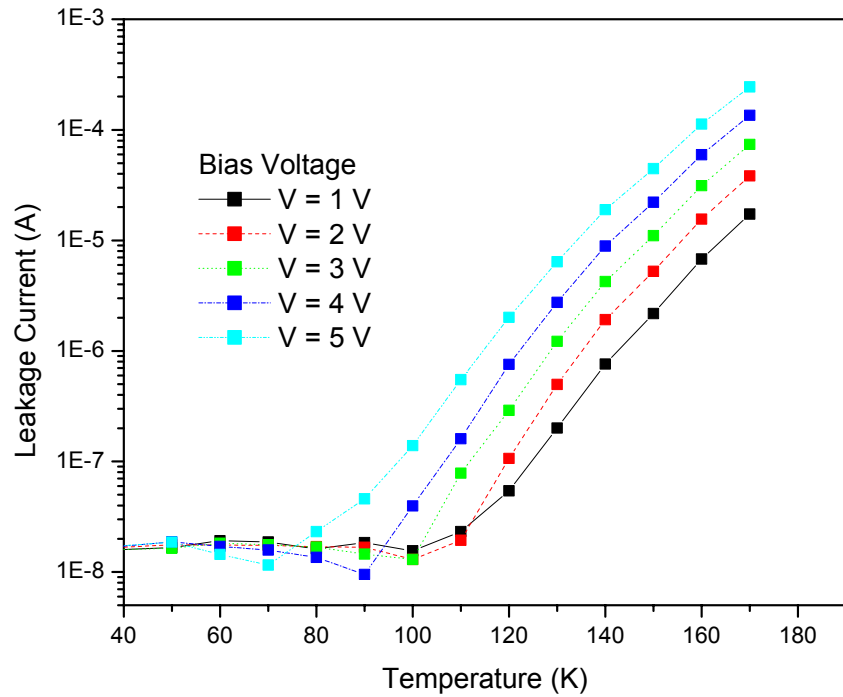


Figure 2.11 Measured leakage (dark) current as a function of temperature for various biases across the device.

The dark current has two major components: the nearly temperature independent tunneling current and the temperature dependent thermionic emission contribution. Therefore, at low temperatures, the tunneling component dominates, making the dark current relatively temperature independent at these temperatures as shown in Fig. 2.10. In addition, we have also found that the onset of thermionic emission current depends on the bias as shown in Fig. 2.11. This is probably due to the lowering of the barrier height relative to the ground state as a result of the bias.

In the following chapter we will present an analysis of the data to estimate the ground state energy and barrier height.

THIS PAGE INTENTIONALLY LEFT BLANK

### III. ANALYSIS

#### A. DARK CURRENT

As discussed in Chapter II, for temperatures below about 80 K the  $I$ - $V$  characteristics are relatively insensitive to temperature. Significant current in this temperature regime is generated by tunneling for bias voltages greater than 5 volts. This behavior is illustrated in Fig. 3.1, which shows a small, steady tunneling current at voltages less than 5 volts. At voltages above 5 volts, however, the current increases rapidly as it becomes easier to tunnel through a reduced barrier.

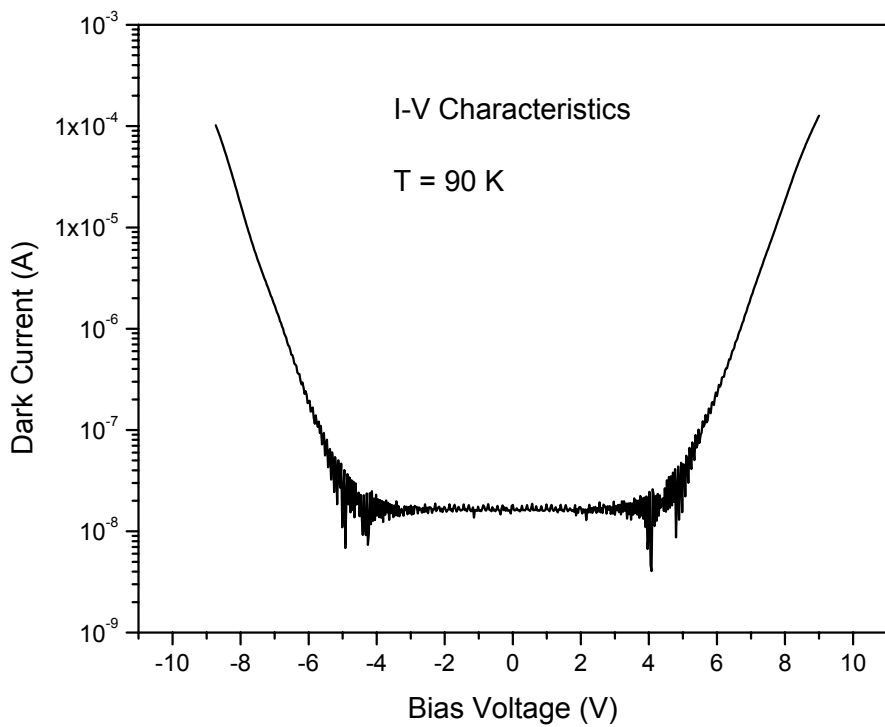


Figure 3.1 Current as a function of bias voltage across the device at 90K.

As illustrated in Fig. 3.2, electrons tunneling under low bias voltage must travel through the entire width of the barrier. As a result of this constant barrier width, a small and nearly constant tunneling current is observed at low bias.

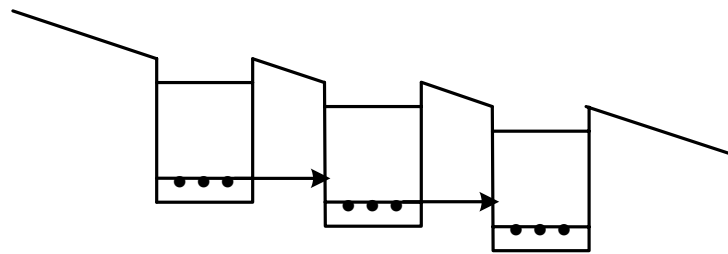


Figure 3.2 Sequential tunneling under low bias voltage.

In the simplified sketch of the bias effect shown in Fig. 3.3, the relative ease of “triangular” tunneling at high bias as compared to low bias voltage is evident. In this case, the effective barrier width is shortened by the high bias effect and consequently a greater tunneling current is observed.

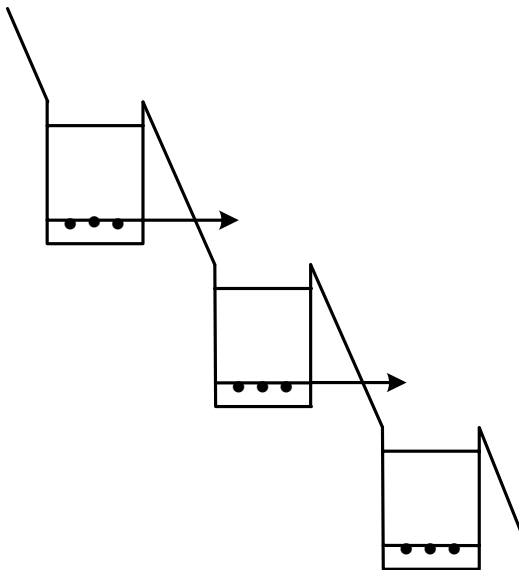


Figure 3.3 Triangular tunneling under high bias voltage.

As seen in Fig. 3.4, as the temperature of our device rises, tunneling current can quickly cease to be the primary contribution to the dark current. Although tunneling current still takes place and continues to be influential at high bias voltages, thermionic emission accounts for the rapid rise in dark current between 100 K to 150 K. Though it is true that tunneling is relatively temperature insensitive, thermally assisted tunneling does take place, accounting for the sharp rise at 4 V of the 100 K (compared to 6 V at 50 K)

curve in Fig. 3.4. Both the tunneling and the thermionic emission contributions to dark current are schematically illustrated in Fig. 3.5.

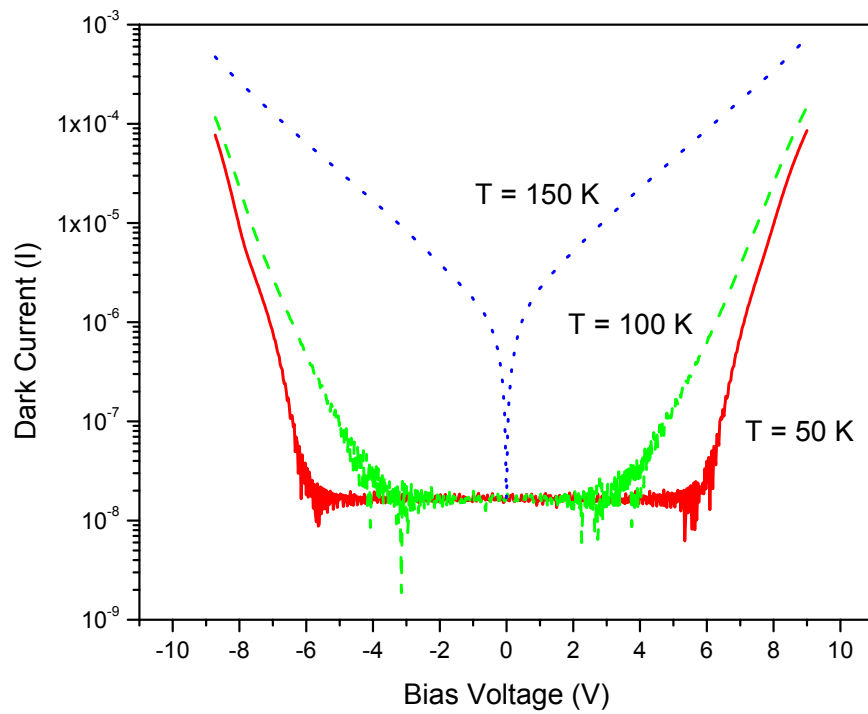


Figure 3.4 Current as a function of bias voltage across the device at 50K, 100K, and 150K.

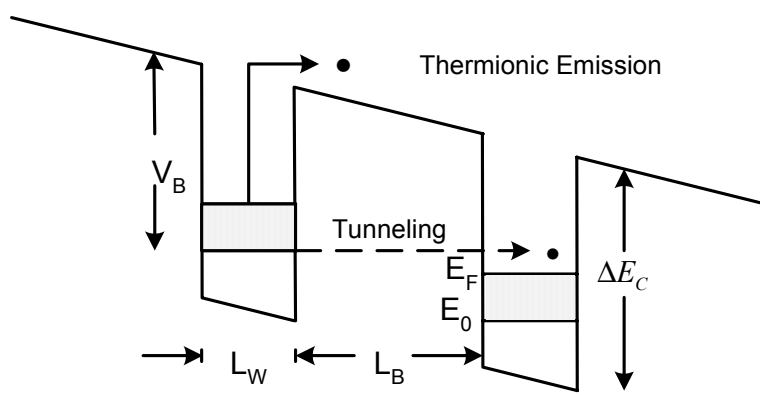


Figure 3.5 Schematic diagram of the quantum well under an external bias showing both tunneling and thermionic processes.

As mentioned, the  $I$ - $V$  characteristics show strong temperature dependence in the high temperature region (above 100 K) as thermionic emission rises with increasing temperature, thereby dominating the relatively temperature-insensitive tunneling current. At low temperatures, however, thermionic emission is greatly reduced and tunneling current is most prominent. For these reasons, a thermionic emission model was chosen to analyze the high temperature region  $I$ - $V$  data.

## B. THERMIONIC EMISSION

Thermionic emission can provide significant information, including an estimation of the conduction band offset and the ground state energy, provided the quasi-Fermi level  $E_F$  (as shown above in Fig. 3.5) of the carriers in the well is known. For low temperatures ( $kT < E_F$ ),  $E_F$  is given by (Karunasiri, 1996)

$$E_F = \frac{n_D \pi \hbar^2 L_w}{m_w^*} \quad (3.1)$$

where  $n_D$  is the density of the carriers in the well,  $\hbar$  is the reduced Planck's constant,  $m_w^*$  is the effective mass of an electron in the well, and  $L_w$  is the width of the well.

To arrive at  $E_F$ , we must first find the two-dimensional density of states,  $g(E)$ , which is defined such that  $g(E)dE$  is the number of states in the energy interval  $E$  to  $(E + dE)$  per unit area of the sample due to free motion of electrons parallel to the layers of the quantum well, as illustrated in Fig. 3.6.

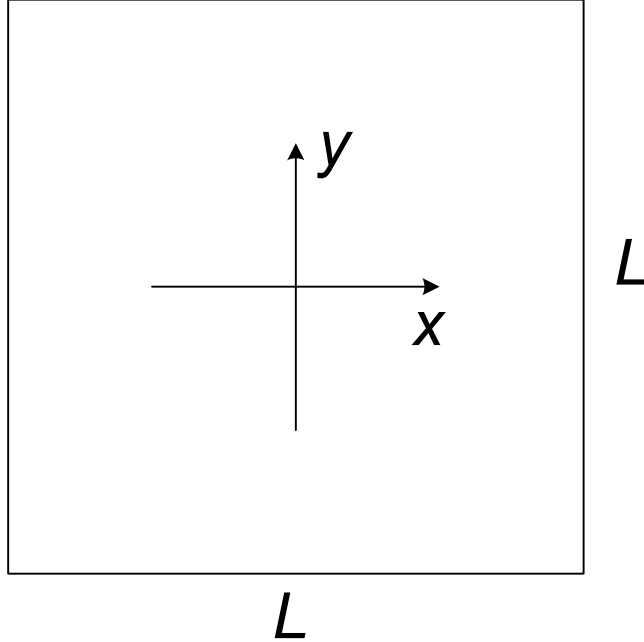


Figure 3.6 Physical dimensions and orientation of the QWIP device where  $L$  represents its lateral dimensions. The layers are grown along the z-direction.

Because electron motion is quantized in the z-direction and they are free to move in the xy plane, the total energy is given by

$$E = E_n + \frac{\hbar^2 k_{xy}^2}{2m_w^*}, \quad (3.2)$$

where  $E_n$  is the quantized energy in the z-direction and  $k_{xy}$  is the wavevector in the xy plane. The wave function for free motion of electrons in the xy plane can be written as

$$\psi = A e^{ik_x x} e^{ik_y y}. \quad (3.3)$$

Imposing the periodic boundary conditions on the wave function  $\psi(x,0) = \psi(x,L)$  and  $\psi(0,y) = \psi(L,y)$ , we find that

$$\begin{aligned} k_x &= n_x \left( \frac{2\pi}{L} \right) \\ k_y &= n_y \left( \frac{2\pi}{L} \right) \end{aligned} \quad (3.4)$$

where  $n_x$  and  $n_y$  are integers and  $L$  is the lateral dimension of the QWIP as shown in Fig. 3.6. For the determination of the density of states, only the  $xy$  term in Eq. (3.6) must be considered. Thus, the allowed  $xy$  energies are given by

$$E = \frac{\hbar^2}{2m_w^*} (k_x^2 + k_y^2) = \frac{\hbar^2}{2m_w^*} \left( \frac{2\pi}{L} \right)^2 (n_x^2 + n_y^2), \quad (3.5)$$

The constant energy contours form circles with radius  $n$ , where  $n^2 = n_x^2 + n_y^2$  as shown in Fig. 3.7.

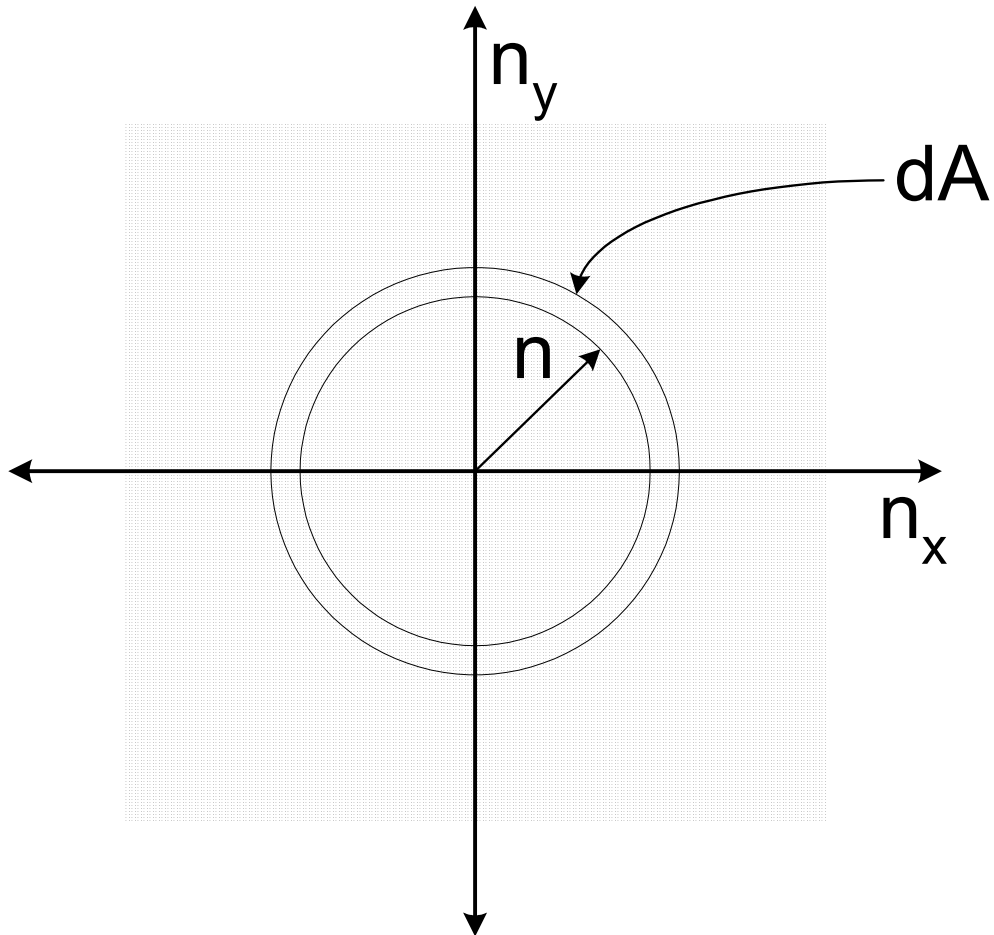


Figure 3.7 Schematic diagram of the two-dimensional density of states.

Now, we would like to generate an expression for the density of states,  $g(E)$ , in the differential area ( $dA$ ) of Fig. 3.7 in which the dots represent available electron states

between  $E$  and  $E + dE$ . Because each energy state occupies unity space in the  $n$ -space, the total number of states between  $E$  and  $E + dE$  is given by

$$G(E)dE = 2 \times 2\pi n d n, \quad (3.6)$$

where the leading factor of two accounts for the spin degeneracy. Using Eq. (3.5) we can rewrite Eq. (3.6) in terms of energy as

$$G(E)dE = 4\pi \frac{m_w^* L^2}{4\pi\hbar^2} dE = L^2 \frac{m_w^*}{\pi\hbar^2} dE. \quad (3.7)$$

Dividing by area (given by  $L^2$ ) we arrive at the following expression for the density of states (i.e., the number of states per unit area over energy):

$$g(E) = \frac{m_w^*}{\pi\hbar^2}. \quad (3.8)$$

To find the quasi-Fermi energy level,  $E_F$ , we must know two-dimensional electron density,  $N_{2D}$ , in the well. This can be easily obtained using the three-dimensional density,  $n_D$ , using the relation

$$N_{2D} = n_D L_w. \quad (3.9)$$

It is often the case that both  $n_D$  ( $\sim 10^{18} \text{ cm}^{-3}$ ) and the well width,  $L_w$ , are known, so that we can find  $N_{2D}$  directly by plugging into Eq. (3.9). The quasi-Fermi Energy can be found by first integrating the density of available states,  $g(E)$ , multiplied by the probability of occupation at a given energy,  $F(E)$ , and equating it to  $N_{2D}$  as follows:

$$N_{2D} = \int_0^\infty F(E)g(E)dE \quad (3.10)$$

In the above integral, the energy is measured from the ground state of the quantum well and the occupation probability is given by the Fermi-Dirac distribution function,  $F(E)$ :

$$F(E) = \frac{1}{1 + \exp\left(\frac{(E - E_F)}{kT}\right)}, \quad (3.11)$$

where  $k$  is Boltzmann's constant and  $T$  is the temperature. Using the Fermi function, the above integral can be written as

$$N_{2D} = \frac{m_w^*}{\pi\hbar^2} \int_0^\infty \left[ \frac{1}{1 + e^{\frac{(E-E_F)}{kT}}} \right] dE = \frac{m_w^*}{\pi\hbar^2} \int_0^\infty \left[ \frac{e^{\frac{-(E-E_F)}{kT}}}{e^{\frac{-(E-E_F)}{kT}} + 1} \right] dE. \quad (3.12)$$

Carrying out the integral and substituting the limits, we find that

$$N_{2D} = kT \frac{m_w^*}{\pi\hbar^2} \left[ \ln(1 + e^{\frac{E_F}{kT}}) \right]. \quad (3.13)$$

Solving for the Fermi energy, we obtain the following:

$$E_F = kT \ln \left[ e^{\frac{\pi\hbar^2 N_{2D}}{kT m_w^*}} - 1 \right]. \quad (3.14)$$

It can easily be seen that when

$$T < \frac{\pi\hbar^2 N_{2D}}{k m_w^*} = T_0, \quad (3.15)$$

the Fermi energy is independent of temperature and is given by

$$E_F = \frac{\pi\hbar^2}{m_w^*} N_{2D}. \quad (3.16)$$

In our experiment, the detector structure was designed having  $\text{In}_{0.1}\text{Ga}_{0.9}\text{As}$  wells with doping density ( $n_d$ ) of  $10^{18} \text{ cm}^{-3}$ . Using Vegard's Law we can interpolate the effective mass of an electron in the  $\text{In}_x\text{Ga}_{1-x}\text{As}$  layer as (Singh, 1993, pp. 185)

$$\frac{1}{m_{\text{In}_x\text{Ga}_{1-x}\text{As}}^*} = \frac{x}{m_{\text{InAs}}^*} + \frac{(1-x)}{m_{\text{GaAs}}^*} \quad (3.17)$$

where  $m_{InAs}^* = 0.028m_e$  and  $m_{GaAs}^* = 0.067m_e$  are the effective masses of electrons in InAs and in GaAs, respectively. This gives a value for the effective mass in the  $In_{0.1}Ga_{0.9}As$  well of  $0.059m_e$ . Using the well width  $L_w = 3.6$  nm we calculate the value of  $N_{2D}$  to be  $3.6 \times 10^{11} \text{ cm}^{-2}$ , while the characteristic temperature ( $T_0$ ) with a constant Fermi energy is found to be about 170 K. Thus, for the temperature range over which the experiment was carried out, the quasi-Fermi energy is independent of temperature.

In order to estimate the dark current it is necessary to estimate the number of thermally excited electrons,  $n(T)$ , above the barrier. This can be obtained from Eq. (3.14) as

$$n(T) = \int_{V_B}^{\infty} F(E)g(E)dE. \quad (3.18)$$

For these electrons,  $E - E_F \gg kT$  and the Fermi function can be approximated by the Boltzmann distribution:

$$F(E) \approx \exp\left(-\frac{(E-E_F)}{kT}\right). \quad (3.19)$$

Thus, the above integral reduces to

$$n(T) = \frac{m_w^* k T}{\pi \hbar^2 L_w} \exp\left(-\frac{(V_B - E_F)}{kT}\right) \quad (3.20)$$

where  $V_B$  is the barrier height measured relative to the ground level.

### C. THERMALLY GENERATED DARK CURRENT

As previously mentioned, our purpose here is to estimate the dark current,  $I(T)$ , generated by the thermal excitation of electrons from the well. The current density is proportional to the number of thermally excited carriers. Thus, the dark current can be estimated from the number of electrons having energies larger than the barrier height and is given by

$$\frac{I(T)}{T} \propto \exp\left(-\frac{(V_B - E_F)}{kT}\right). \quad (3.21)$$

From this last expression we can find the activation energy  $V_B - E_F$  by plotting  $\ln\left[\frac{I(T)}{T}\right]$  versus  $1/T$ . Fig. 3.8 shows the Arrhenius plot for measured current at 2 V bias for temperatures in the 110 – 170 K range.

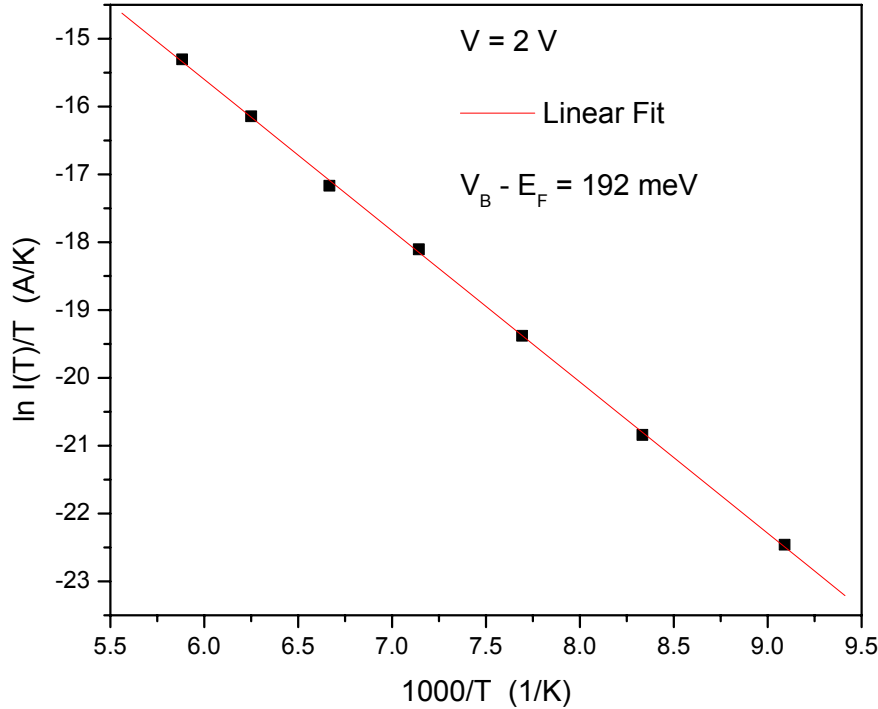


Figure 3.8 Arrhenius plot of the leakage current. The straight line indicates the thermionic nature of the current in the high temperature region.

The excellent linear fit to the data indicates the validity of Eq. (3.21) for describing the dark current. The slope of the line  $\left[ \frac{(V_B - E_F)}{1000k} \right]$  can be used for the estimation of the activation energy  $V_B - E_F$ . For the determination of the ground state energy it is necessary to find the barrier height,  $V_B$ , at zero bias, as well as the Fermi energy.

The condition that  $kT < E_F$  allows us to estimate the Fermi energy using Eq. (3.1). We find that

$$E_F = \frac{n_D \pi \hbar^2 L_w}{m_w^*} \cong 15 \text{ meV}. \quad (3.22)$$

In order to find  $V_B$  at zero bias, we have repeated the plot of  $\ln[I(T)/T]$  vs.  $1/T$  for several bias voltages. The results are summarized in Table 3.1.

Bias Voltage (V)	1.0	1.5	2.0	2.5	3	3.5	4.0	4.5	5.0
$V_B - E_F$ (meV)	199	194	192	185	181	175	168	161	160

Table 3.1 Bias voltages and corresponding activation energies  $V_B - E_F$ .

Fig. 3.9 shows the plot of activation energies ( $V_B - E_F$ ) as a function of bias voltages as given in Table 3.1. The data in Table 3.1 can be fitted to a straight line and the y-intercept gives the activation energy at zero bias, which is approximately equal to 211 meV.

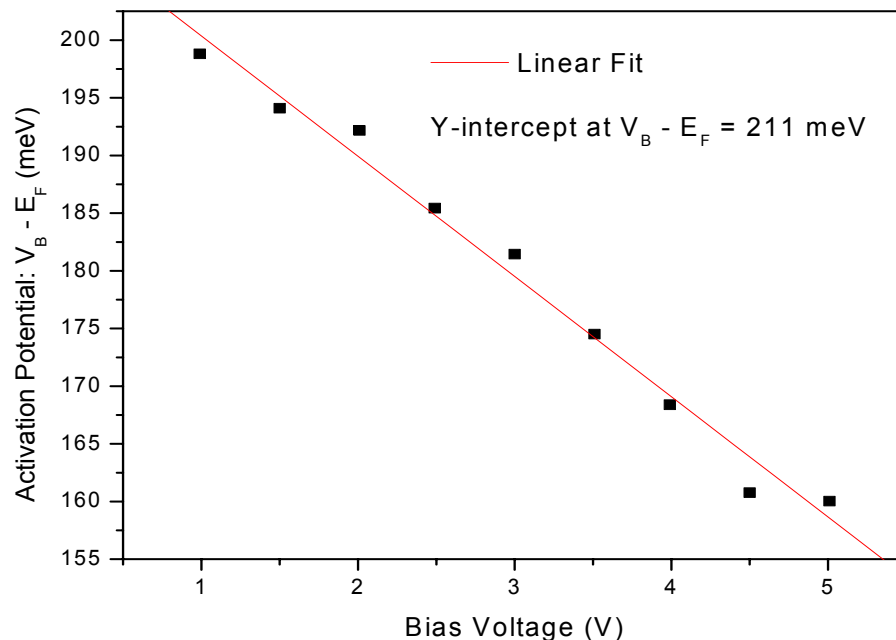


Figure 3.9 Linear fit of the activation energies over a range of voltages.

Given that our zero bias activation energy is 211 meV,  $V_B$  corresponding to the zero bias condition is approximately 226 meV. However, this is as far as we can go experimentally: the problem remains of how to estimate the conduction band offset. For this calculation  $E_0$  must be known, but paradoxically it seems that  $E_0$  cannot be estimated without the offset. In order to overcome this obstacle, we make use of the fact that the maximum energy of the ground state,  $E_0^{\max}$ , occurs when the barrier height is infinite. In this case,  $E_0$  is given by

$$E_0^{\max} = \frac{\hbar^2}{2m_w^*} \left( \frac{\pi}{L_w} \right)^2. \quad (3.23)$$

Using the given values of well width and effective mass, we find  $E_0^{\max}$  to be approximately 490 meV. Because  $V_B$  is the height relative to the ground state, the upper bound of the conduction band offset,  $\Delta E_C^{\max}$ , must be given by

$$\Delta E_C^{\max} = V_B + \frac{\hbar^2}{2m_w^*} \left( \frac{\pi}{L_w} \right)^2 = V_B + 490 \text{ meV}. \quad (3.24)$$

The physical situation is given schematically in Fig. 3.10.

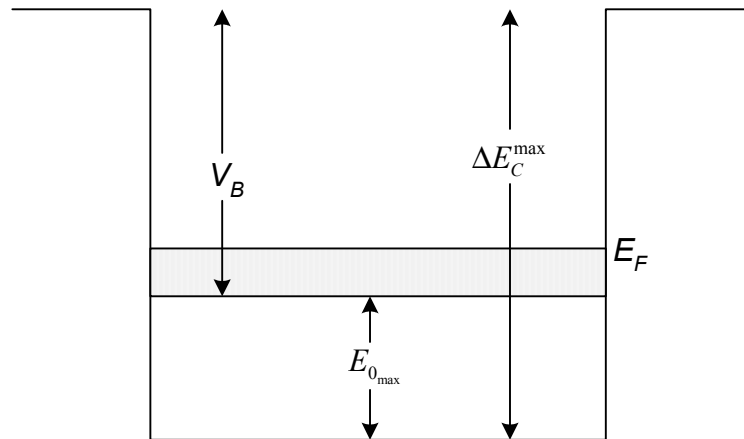


Figure 3.10 Conceptual diagram of the conduction band offset,  $\Delta E_{C_{\max}}$ .

Using this relation, in which we know  $V_B$  experimentally and begin with the infinite approximation of  $E_0^{\max}$ , we can numerically calculate the ground state energy corresponding to the band offset of  $\Delta E_C^{\max}$ . Then, a new value for the conduction band offset can be calculated by adding the  $V_B$  to the ground state energy calculated using the  $\Delta E_C^{\max}$ . This iterative procedure (Karunasiri, G., 1996) is continued until convergence is obtained, providing both the band offset and ground state energy for a given  $V_B$ . As previously discussed,  $V_B$  can be determined using the measured  $I$ - $V$  data while the Fermi energy,  $E_F$ , can be estimated using device parameters. The method was carried out using a Matlab program that is described in detail in the Appendix.

Using the iterative approach just described, the conduction band offset  $\Delta E_C$  and the ground state energy  $E_0$  are found to be 362 meV and 136 meV, respectively. To check the validity of this data we can make use of the generally accepted approximation of the conduction band offset between AlGaAs and InGaAs:

$$\Delta E_C = 0.6(E_g^{AlGaAs} - E_g^{InGaAs}) \quad (3.25)$$

To find these values of  $E_g$  we use the following formulas (Casey and Panish, 1978), which correspond to energy gap compositional dependence at 300 K:

Compound	$E_g$ (eV)
$Al_xGa_{1-x}As$	$1.424 + 1.247x$
$Ga_xIn_{1-x}As$	$0.36 + 1.064x$

Table 3.2 Formulas for the energy bandgaps of AlGaAs and InGaAs compounds.

In this way we find the  $E_g$  ( $Al_xGa_{1-x}As$ ) to be 1.885 eV while the  $E_g$  ( $Ga_xIn_{1-x}As$ ) is 1.32 eV. Using equation (3.25), we find that the empirical offset is about 340 meV. This estimation is found to be well within 5% of our experimental value of roughly 360 meV. The following schematic in Fig. 3.11 displays the various energy values within the quantum well structure derived from our experiment:

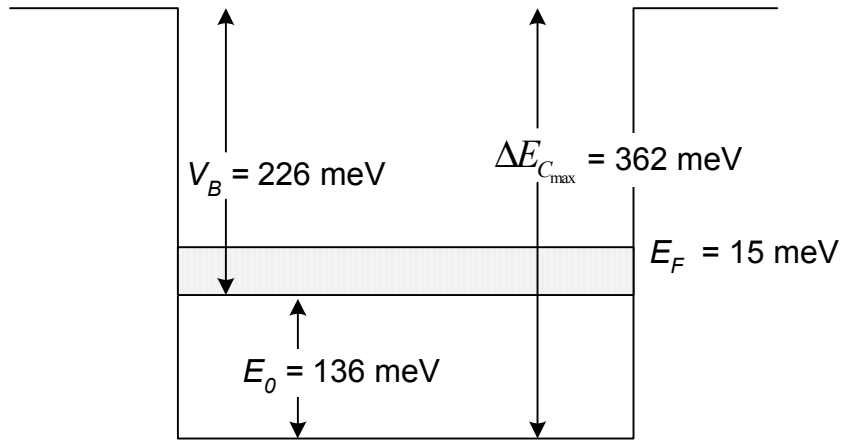


Figure 3.11 Estimated ground state energy and conduction band offset using the thermionic emission analysis.

#### D. DETECTIVITY ( $D^*$ ) AS A FUNCTION OF TEMPERATURE

There are two important parameters used for the quantification of the performance of photodetectors: responsivity and detectivity. The responsivity is the output current produced per watt of radiant optical power input,

$$R = \frac{I_p}{\Phi_p} \quad [A/W], \quad (3.26)$$

where  $I_p$  is the photocurrent and  $\Phi_p$  is the incident power on the device. As our experiment is carried out in the dark condition, we utilize previously measured values for the responsivity,  $R$ , for the same QWIP (Zhou, 2002). Fig. 3.12 displays the photoresponse of the device as a function of wavelength. The peak of the responsivity appears at 5  $\mu\text{m}$ . Table 3.3 is also included, and contains additional device data found by Zhou *et al.*

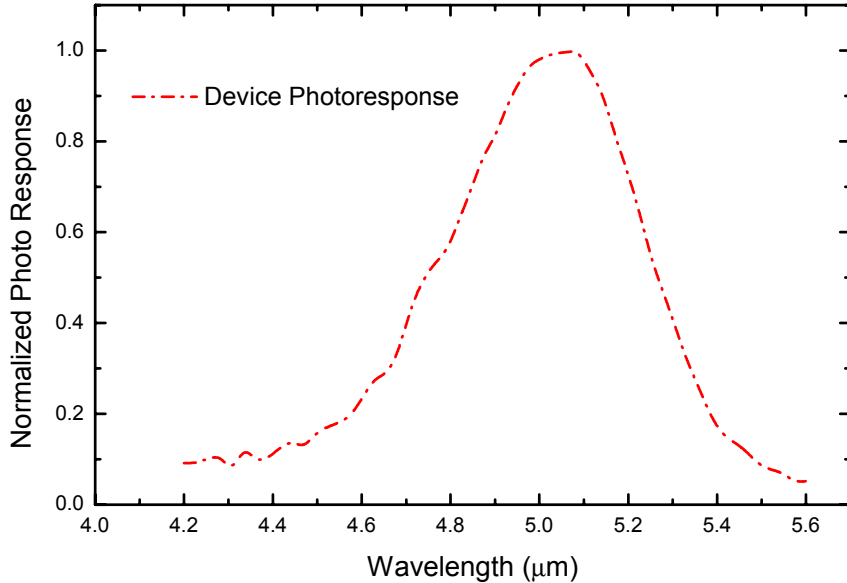


Figure 3.12 Photoresponse of detector at various wavelengths.

Transition Type	Peak Absorbance	Dark Current at 1.5 V, 20 k	Window Current at 1.5 V, 20 K	Peak Width of Photoresponse Curve	Integrated Responsivity At 2 V
B-C	$1510 \text{ cm}^{-1}$	$2 \times 10^{-10} \text{ A}$	$2 \times 10^{-9} \text{ A}$	26 meV	20 mA/W

Table 3.3 Device information provided by the optical experiments done by Zhou.

We estimate the sensitivity of the detector by estimating its detectivity. The detectivity of a device is a measure of the smallest photon flux that can be measured, and it is therefore dependent on detector noise. Detectivity is defined as

$$D^* = \frac{\sqrt{A\Delta f}}{NEP} \quad [\text{cm}\sqrt{\text{Hz}}/\text{W}], \quad (3.27)$$

where the  $NEP$  (noise equivalent power) is the root-mean-square (rms) incident radiant power that gives a photosignal equal to the noise (or signal-to-noise ratio of one),  $A$  is the area of the detector, and  $\Delta f$  is the bandwidth of the amplifier used. Since a QWIP is effectively a photoconductor, the predominant noise comes from the generation-

recombination of carriers. The generation-recombination noise current ( $i_N$ ) can be estimated using the measured dark current as

$$i_N = \sqrt{4eGI_d\Delta f}, \quad (3.28)$$

where  $e$  is the electron charge,  $G$  is the optical gain, and  $I_d$  is the temperature dependent dark current (Levine, 1993, pp. R25). Using Eq. (3.26), with  $\Phi_p = NEP$ , the noise equivalent power can be obtained using the measured responsivity as

$$NEP = \frac{i_N}{R}. \quad (3.29)$$

After incorporating these values for  $i_N$  and the  $NEP$  into Eq. (3.27), we find that

$$D^* = \frac{\sqrt{A}}{\sqrt{4eGI_d}} R. \quad (3.30)$$

With a 1.5 volt bias across the device,  $R$  at 5  $\mu\text{m}$  is found to be 0.030 A/W. The area of the device is 200  $\mu\text{m}$  by 200  $\mu\text{m}$ , and as such  $\sqrt{A}$  equals 200  $\mu\text{m}$ . The commonly accepted value for gain in a QWIP device is 0.1 (Levine, 1993, pp. R26). With these details in mind, the plot of the detectivity versus temperature was created and is shown in Fig. 3.13. The variable in  $D^*$  is the temperature dependent dark current at different bias voltages.

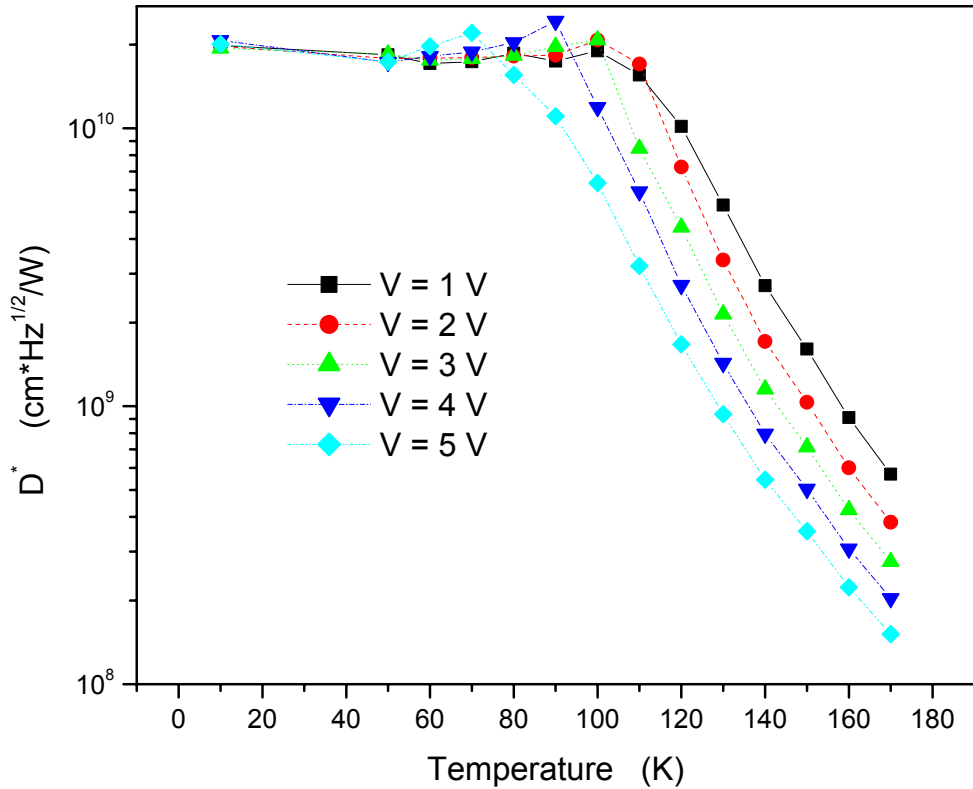


Figure 3.13 Detectivity at  $5\text{ }\mu\text{m}$  versus temperature for set of bias voltages.

It can be seen from Fig. 3.13 that the detectivity remains constant up to 100 K for low bias voltages (less than 3 V). However, for bias voltages greater than 3 V the detectivity degrades beyond 80 K due to excessive thermionic assisted tunneling. In addition, at high temperatures (greater than 100 K) the detectivity drops rapidly due to the exponential increase of the thermionic emission current. This measurement indicates that the present device is not suitable for high quality imagery if the operating temperature is beyond 80 K.

THIS PAGE INTENTIONALLY LEFT BLANK

## IV. CONCLUSIONS

The I-V characteristics of a bound-to-continuum QWIP device with  $\text{Al}_{0.37}\text{Ga}_{0.63}\text{As}$  barriers of 23 nm,  $\text{In}_{0.1}\text{Ga}_{0.9}\text{As}$  wells of 3.6 nm, and a doping density ( $n_d$ ) of  $10^{18} \text{ cm}^{-3}$  were gathered and analyzed for various temperatures. The device was cooled using a closed cycle refrigerator and the data were analyzed using the Agilent 4155B Semiconductor Parameter Analyzer. At low temperatures the leakage (dark) current is dominated by sequential tunneling through the ground states, while at high temperatures we employ a thermionic emission model with which we can estimate the barrier height of the wells. With this value for the barrier height we employed an iterative Matlab program to establish the energy levels within the well. The estimated conduction band offset of 360 meV is in good agreement with the empirical value of 340 meV assuming 60% of the total band offset appears in the conduction band. Two useful figures of merit were discussed: responsivity and detectivity. An expression for the detectivity of the device was derived as a function of dark current. Using the measured dark current, the detectivity was estimated as a function of the temperature. This allowed us to determine the suitable operating temperature range of the device to be between 0 and 80 K.

The details of the laboratory setup and test system and process are included with the intent to provide future students with simple and comprehensive procedural insight.

THIS PAGE INTENTIONALLY LEFT BLANK

## LIST OF REFERENCES

1. Blair, Dr. Bill, "Johns Hopkins University spectroscopy." [[http://violet.pha.jhu.edu/~wpb/spectroscopy/em\\_spec.html](http://violet.pha.jhu.edu/~wpb/spectroscopy/em_spec.html)]. March, 1999.
2. Casey, H. C., Jr., and M. B. Panish, *Heterostructure Lasers, Part A, Fundamental Principles, Part B, Materials and Operating Characteristics*, Academic Press, New York, 1978.
3. Chiu, L. C., J. S. Smith, S. Margalit, A. Yariv, and A. Y. Cho, *Infrared Phys.* **23**, pp. 93, 1983.
4. Coon, D. D. and R.P.G. Karunasiri, "New Mode of IR detection using quantum wells," *App. Phys. Lett.*, **45**, pp. 649 ~ 651, 1984.
5. Coon, D. D., R. P. G. Karunasiri, and L. Z. Liu, "Narrow band infrared detection in multiquantum well structures," *App. Phys. Lett.*, **47**, pp. 289 ~ 291, 1985.
6. Esaki, L. and R. Tsu, *IBM Research Note*, RC - 2418, 1969.
7. Esaki, L. and H. Sasaki, *IBM Tech. Disc. Bull.*, **20**, pp. 2456, 1977.
8. Fraunhofer Institute for Applied Solid-State Physics (IAF) website, 2001.
9. Gunapala, S. D., J. K. Liu, M. Sundaram, S. V. Bandara, C. A. Shott, T. Hoelter, P. D. Maker, and R. E. Muller, "Long Wavelength Quantum Well Infrared Photodetector (QWIP) Research at Jet Propulsion Laboratory," *Proc. SPIE*, **2744**, pp. 722 ~ 730, 1996.
10. Gunapala, SD, Choi, KK, Bandara, SV, Liu, WK, and Fastenau, JM, "Detection wavelength of InGaAs/AlGaAs quantum wells and superlattices," *J. Appl. Phys.*, **91**, pp. 551-564, 2002.
11. Hasnain, G., B. F. Levine, S. Gunapala, and N. Chand, "Large photoconductive gain in quantum well infrared detectors," *Appl. Phys. Lett.*, **57**, pp. 608 ~ 610, 1990.
12. Karunasiri, R. P. G., J. S. Park, J. Chen, R. Shih, J. F. Scheihing, and M. A. Dodd, "Normal incident InGaAs/GaAs multiple quantum well infrared detection using electron intersubband transitions," *Appl. Phys. Lett.*, **67**, pp. 2600 ~ 2602, 1995.
13. Karunasiri, G., "Thermionic emission and tunneling in InGaAs/GaAs quantum well infrared detectors," *J. Appl. Phys.*, **79**, pp. 8121 ~ 8123, 1996.

14. Kasap, S. O., Principles of Electronic Materials and Devices, 2<sup>nd</sup> Ed., pp. 262, McGraw-Hill, c 2002.
15. Kinch, M. A. and A. Yariv, "Performance limitations of GaAs/AlGaAs infrared superlattices," *App. Phys. Lett.*, **55**, pp. 2093 ~ 2095, 1989.
16. Levine, B. F., K. K. Choi, C. G. Bethea, J. Walker, and R. J. Malik, "New 10μm infrared detector using intersubband absorption in resonant tunneling GaAlAs superlattices," *App. Phys. Lett.*, **50**, pp. 1092 ~ 1094, 1987.
17. Levine, B. F., A. Zussman, S. D. Gunapala, M. T. Asom, J. M. Kuo, and W. S. Hobson, "Photoexcited escape probability, optical gain, and noise in quantum well infrared photodetectors," *J. Appl. Phys.*, **72**, pp. 4429 ~ 4443, 1991.
18. Levine, B. F., "Quantum-well infrared photodetectors," *J. Appl. Phys.*, **74**, pp. R1-R81, 1993.
19. Singh, J., Physics of Semiconductors and their Heterostructures, pp. 285, McGraw-Hill, c 1993.
20. Smith, J. S., L. C. Chiu, S. Margalit, A. Yariv, and A. Y. Cho, "A new infrared detector using electronic emission from multiple quantum wells," *J. Vac. Sci. Technol. B* **1**, pp. 376 - 378, 1983.
21. West, L. C. and S. J. Eglash, "First observation of an extremely large-dipole infrared transition within the conduction band of a GaAs quantum well," *App. Phys. Lett.*, **46**, pp. 1156 ~ 1158, 1985.
22. Yu, L. S. and S. S. Li, "A metal grating coupled bound-to-miniband and transition GaAs multiquantum well/superlattice infrared detector," *Appl. Phys. Lett.*, **59**, pp. 1332 ~ 1334, 1991.
23. Zhou, L, "Fabrication of quantum well detector array for thermal imaging," M.Eng. thesis, Natuional University of Singapore, 2002

## APPENDIX. [PROGRAM NOTES]

The following procedure describes the numerical estimation of the ground state energy of a finite quantum well. Fig. A.1 shows the ground state energy level and wavefunction in a finite potential well

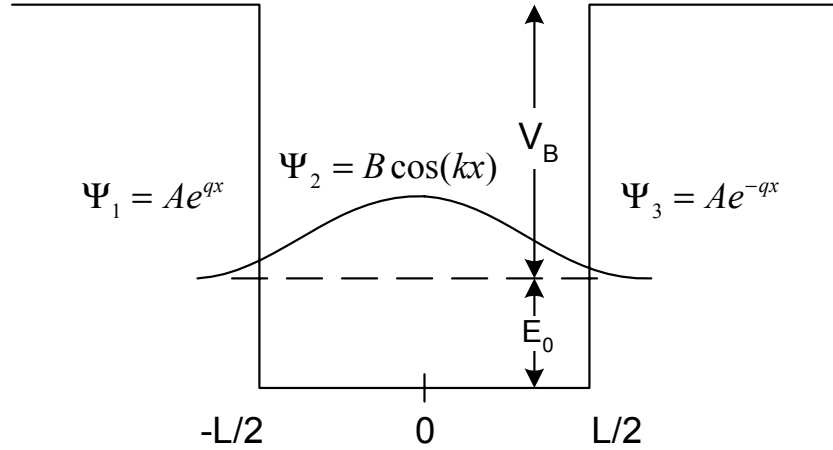


Figure A.1 Energy state and wavefunction in finite potential well. The finite well is extensively utilized in the design of semiconductor devices, particularly in quantum well based devices.

$$\text{where } q = \sqrt{\frac{2m_B^*}{\hbar^2}(V - E)} \text{ and } k = \sqrt{\frac{2m_W^*}{\hbar^2}E} .$$

Given the requirement that the wavefunctions and their derivatives must match at their boundaries we find that

$$A \cos(kL/2) = C e^{-qL/2} \quad (\text{A.1})$$

and

$$-\frac{1}{m_W^*} A k \sin(kL/2) = -\frac{1}{m_B^*} C q e^{-qL/2} . \quad (\text{A.2})$$

By dividing Eq. (4.2) by Eq. (4.1) we find the following to be true:

$$-\frac{k}{m_W^*} \tan(kL/2) = -\frac{1}{m_B^*} q . \quad (\text{A.3})$$

After substitution (for  $k$  and  $q$  in terms of energy) and simplification we find that the ground state energy must satisfy

$$\sqrt{\frac{E}{m_w^*}} \tan \sqrt{\frac{m_w^* L^2}{2\hbar^2} E} = \sqrt{\frac{(V-E)}{m_B^*}} \quad (\text{A.4})$$

Since the value of  $V$  is unknown, we begin with the maximum possible value (as discussed in the text) and cyclically narrow down the value of the offset until it converges on the actual value. We have created the following program in Matlab to calculate the conduction band offset and ground state energy for a given  $V_B$ . Parameters for any rectangular quantum well can be used as inputs for the calculation of the offset.

```

clc
clear all

Vb = 0.2254; %[eV]
m_e = 9.11e-31; %[kg]
hbar = 1.055e-34; %[J*s]
Eapprox(1) = 0.492; %[eV]
L = 3.6e-9; %[m]
J = L/2; %[m]
q = 1.602e-19; %[C]

m_effw = 0.059*m_e; %[kg]
m_effb = 0.084*m_e; %[kg]
Vapprox(1) = Eapprox(1) + Vb;
for n = 2:1:10000
    a = 1;
    y = 0;
    for E = 0.001:0.001:Vapprox(n-1);
        AA = sqrt((E*q)/m_effw);
        AB = sqrt((2*m_effw*E*q*(J^2))/(hbar^2));
        AC = sqrt(((Vapprox(n-1) - E)*q)/m_effb);

        P = AA*tan(AB) - AC;

        z = y;
        y = P;
        if z.*y < 0
            Eout(a) = E;
            a = a+1;
        end
    end
    Eapprox(n) = Eout(1);
    Vapprox(n) = Eapprox(n) + Vb;
    if Vapprox(n) == Vapprox(n-1)
        disp(Vapprox(n))
    end
end

```

```
break  
end  
end
```

THIS PAGE INTENTIONALLY LEFT BLANK

## **INITIAL DISTRIBUTION LIST**

1. Defense Technical Information Center  
Ft. Belvoir, Virginia
2. Dudley Knox Library  
Naval Postgraduate School  
Monterey, California
3. Chairman (Code PH)  
Department of Physics  
Naval Postgraduate School  
Monterey, California
4. Gamani Karunasiri  
Naval Postgraduate School  
Monterey, California
5. James Luscombe  
Naval Postgraduate School  
Monterey, California
6. Ensign Thomas R. Hickey  
United States Navy  
73 Greenbush Street  
Cortland, New York